



# Clinopyroxene diversity and magma plumbing system processes in an accreted Pacific ocean island, Panama

Sander M. Molendijk<sup>1</sup> · David M. Buchs<sup>2,3</sup> · Paul R. D. Mason<sup>1</sup> · Jonathan D. Blundy<sup>4</sup>

Received: 23 July 2021 / Accepted: 18 January 2022  
© The Author(s) 2022

## Abstract

Characterising equilibrium and disequilibrium crystal-melt processes is critical in determining the extent of magma mixing and crystallization conditions in the roots of volcanoes. However, these processes remain poorly investigated in most Pacific intraplate ocean settings that are difficult to access and study. To help address this issue, we investigated crystallization conditions of clinopyroxene phenocrysts in an accreted Palaeogene oceanic island in Panama. Petrographic and geochemical observations, petrological modelling of major and trace elements, and liquid-mineral multicomponent equilibrium tests were carried out using basalts, picrites, and hawaiites of the transitional tholeiitic shield to alkaline post-shield volcanic stages of the island. Five types of clinopyroxene crystals were identified, including (1) microphenocrysts with micron-scale oscillatory zoning, (2) primitive, yet resorbed picrite-hosted phenocrysts, (3) chemically homogeneous, anhedral crystals found in the remaining basalts, (4) Ti-rich euhedral hawaiite-hosted phenocrysts, and (5) evolved sector-zoned phenocrysts. Liquid-clinopyroxene multicomponent equilibrium tests in combination with textural analysis show that ~74% of the studied clinopyroxenes are in possible major element equilibrium with one of the available whole rock magma compositions, of which only 21% are equilibrated with their carrier liquid. To deconvolute clinopyroxene-melt pairings and determine plumbing system conditions, we combine rhyolite-MELTS modelling, geothermobarometry, and major- and trace-element equilibrium evaluations, limiting crystallization conditions to crustal levels (<23 km depth). No migration of magmatic reservoirs to deeper levels is observed during the shield- to post-shield transition. These results suggest the occurrence of an extensive crystal mush system during the late shield to post-shield volcanic stages of this intraplate volcanic system, with both primitive and evolved crystallization domains sampled during eruptions.

**Keywords** Geothermobarometry · Cumulate recycling · Clinopyroxene zoning · Magma mixing

## Introduction

Equilibrium crystallization is a fundamental assumption in petrological studies to quantify P–T and  $fO_2$  conditions of a magmatic plumbing system (Putirka 2008). This assumption allows one to apply experimentally determined parameters, such as crystal-liquid partition coefficients, to natural systems, and thus predict petrological conditions of magmatic reservoirs (e.g., Neave and Putirka 2017; Vander Auwera et al. 2019). However, resolving state variables from crystal-liquid partitioning requires knowledge of two unknowns: the crystal chemistry and the composition of the coexisting equilibrium melt. This is where a discrepancy is commonly found between experimental and natural systems, because the former is limited to closed systems, whereas natural magmatic systems frequently comprise multi-reservoir, open systems subject to mixing, mush entrainment, and

---

Communicated by Othmar Müntener.

✉ Sander M. Molendijk  
sander.molendijk@kuleuven.be

<sup>1</sup> Department of Earth Sciences, Utrecht University, Princetonlaan 8A, 3584 CB Utrecht, The Netherlands

<sup>2</sup> School of Earth and Environmental Sciences, Cardiff University, Main Building, Cardiff CF19 3AT, UK

<sup>3</sup> Smithsonian Tropical Research Institute, Panama City, Panama

<sup>4</sup> Department of Earth Sciences, University of Oxford, South Parks Road, Oxford OX1 3AN, UK

replenishment events (e.g., Dobosi and Fodor 1992; Nakamura 1995; Marsh 1996; Costa et al. 2010). As a consequence, it is often unclear whether whole-rock data represent distinct melt batches with equilibrated crystal contents or end-products of complex mixing, accumulation, and/or disequilibrium crystallization processes (Neave and Putirka 2017), especially when crystallinity is high.

Assessing the nature of magmatic processes in intraplate ocean volcanoes is made additionally challenging because of difficulties in accessing and sampling lower stratigraphic levels of seamounts and oceanic islands. Thus, most of our knowledge of these widely occurring, yet poorly explored, volcanic systems is heavily skewed towards the study of easily accessible and especially large (partly subaerial) volcanic systems such as those of Hawaii, Iceland, Galapagos, and Canary islands (Putirka 1997; Klügel et al. 2005; Stroncik et al. 2009; Tornare et al. 2016; Neave and Putirka 2017). However, these systems may not be a representative sample of the far larger population of comparatively smaller intraplate ocean volcanoes (Woodhead 1992; Davis et al. 2002; Konter et al. 2009; Buchs et al. 2018a, b). In addition, whereas intraplate ocean islands on the slow-moving Atlantic Plate have been studied in greater detail due to their better and more prolonged exposure, magmatic processes in islands formed on the fast-moving Pacific Plate could be partly distinct, but testing this hypothesis is commonly hampered by fast subsidence that makes them more difficult to access and study.

Here, we address this gap in understanding of ocean islands on the Pacific plate by providing novel petrographic, geochemical and petrological constraints on equilibrium and disequilibrium conditions in the plumbing system of an accreted Palaeocene intraplate ocean volcano in the Azuero Peninsula, Panama. Our assessment of crystal (clinopyroxene) and melt (whole-rock) chemical exchange reveals clear evidence for substantial mixing and crystal mobility in all samples of the shield to post-shield volcanic stages of the accreted island. In many cases, disequilibrium with carrier liquids can be readily recognised from petrographic observations alone (e.g., mineral resorption textures), but in other instances disequilibrium, it is more cryptic and only recognisable through careful, multicomponent equilibrium tests.

## Geological setting

The studied accreted oceanic island ('Hoya Island') is part of the Azuero Accretionary Complex on the Azuero Peninsula (Fig. 1), previously identified on the basis of lithostratigraphic field constraints, geochronological and biochronological data, and relative enrichment in incompatible elements with respect to other accreted oceanic complexes in Central America (Buchs et al. 2011). Hoya

Island occurs as fragments of a Palaeocene intraplate volcano and includes a well-preserved (composite) stratigraphic transition from shield to post-shield and post-erosional volcanic stages (Buchs et al. 2011), as commonly observed in large intraplate oceanic volcanoes elsewhere (Clague and Dalrymple 1987; Konter et al. 2009; Staudigel and Clague 2010). The age of formation of the island is well supported by Ar–Ar step heating results that have well-constrained plateau ages between  $61.0 \pm 0.3$  and  $64.6 \pm 0.3$  Ma (Gazel et al. 2018). Older and younger Ar–Ar ages from the studied accreted sequences (Hoernle et al. 2002; Gazel et al. 2018), are in disagreement with field and biostratigraphic data (Buchs et al. 2011), and/or show evidence for disturbance by post-crystallization alteration. Igneous rocks of Hoya Island include transitional tholeiitic picrites and basalts, and (alkaline) hawaiites that define a chemical trend from high to low Mg# ( $100 \cdot \text{Mg} / (\text{Mg} + \text{Fe})$ ), associated with an increase in  $\text{TiO}_2$  and La/Yb ratios (Buchs et al. 2011). Picrites, interlayered with basalt lavas, were emplaced in submarine to subaerial environments during the shield stage, whereas hawaiites were only found in subaerial sequences above basaltic conglomerates on top of shield sequences, or as dykes crosscutting shield-stage basalts. Because of this stratigraphic relationship (e.g., well exposed in Puerto Escondido in the SW Azuero Peninsula) and the distinct chemical composition of the hawaiites relative to the picrites and basalts, the hawaiites have been interpreted as a record of post-shield stage volcanism (Buchs et al. 2011).

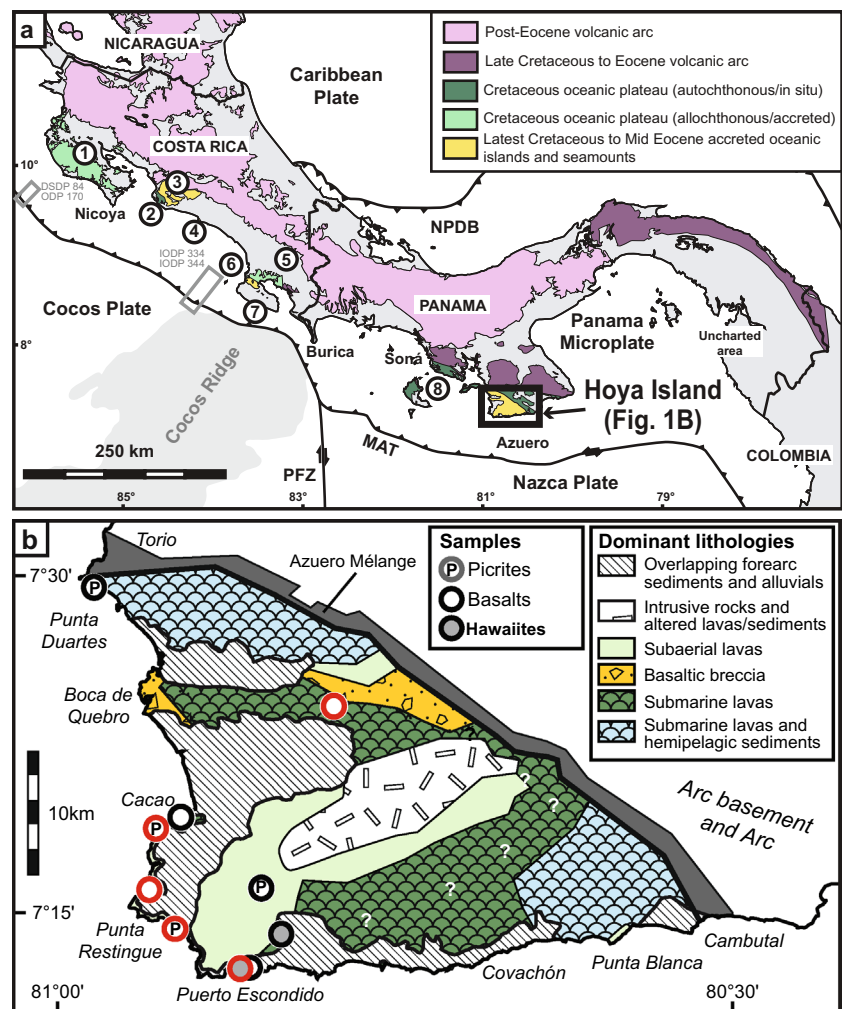
## Materials and methods

Our characterisation of the plumbing system of Hoya Island combines previous geological and geochemical constraints (Buchs et al. 2011) with new sampling, petrographic analysis, and geochemical modelling. Samples were selected from the shield and post-shield volcanic stages on the basis of field stratigraphic constraints (Buchs et al. 2011, Fig. 1). The degree of equilibrium between whole-rock and phenocrysts was evaluated as a prelude to equilibrium-based geothermobarometric calculations and rhyolite-MELTS modelling. Temperatures and pressures of crystallization were determined for equilibrated phenocryst-melt pairs that were then compared to those inferred from bulk-rock geochemical modelling.

## Samples

Four picrite, three basalt, and three hawaiite samples of lavas and dykes were selected from the Azuero Accretionary Complex to study the plumbing system of Hoya island (Figs. 1 and 2, Supplementary Materials 1, Fig. S1; Supplementary Materials 2). These samples were originally collected by

**Fig. 1** Geological setting of the studied Palaeocene–Early Eocene oceanic island accreted and exposed on Azuero Peninsula. **a** Simplified geological map of the Costa Rica–Panama convergent margin (modified from Buchs et al. 2010), with Cretaceous to Cainozoic igneous units and accretionary complexes exposed in the forearc: (1) Nicoya Complex, Manzanillo Terrane, and Tortugal komatiitic suite; (2) Herradura Complex; (3) Tulin Formation; (4) Quepos terrane; (5) Inner Osa Igneous Complex; (6) Outer Osa Igneous Complex; (7) Osa Mélange; and (8) Azuero Plateau, Azuero Accretionary Complex and Mélange. MAT=Middle America Trench, NPDB=North Panama Deformed Belt, and PFZ=Panama Fracture Zone. **b** Simplified geological map of the Azuero Accretionary Complex with the location of the studied igneous rocks in Hoya Island (modified from Buchs et al. 2011). Samples with whole-rock and clinopyroxene geochemical data are shown in red



Buchs et al. (2011), except for hawaiite PA14-032, collected in 2014 (P.O. Baumgartner, pers. com. 2015) and analysed at Cardiff University (Supplementary Materials 2). The samples were chosen based on their freshness and compositional range to provide a representative insight into petrological processes of Hoya Island. Alteration in the selected samples was minor (LOI=0.4–5 wt.%) and primarily affects matrix phases. Higher LOI (> 3 wt.%) is explained by abundant glass and olivine that was partly affected by hydrous alteration. Polished thin sections of these samples (100  $\mu\text{m}$  thickness) were prepared at Cardiff University for SEM, microprobe, and LA-ICP-MS analyses.

## Analytical methods

### Scanning electron microscope mapping

SEM EDS mapping procedures were performed using the Zeiss Sigma HD field emission SEM at Cardiff University. Element maps as well as BSE images were acquired at 20 kV with a 120  $\mu\text{m}$  diameter final aperture and a nominal beam

current of ~4 nA. Process time for element maps was set to 0.5 microseconds. Element concentrations were measured using dual 150 mm<sup>2</sup> Oxford Instruments X-Max EDS silicon drift detectors with process time set to 2 microseconds and a dead time of ~60%. Dwell time for elemental maps and BSE images were 15 and 10 ms, respectively. Beam drift was measured every 30 min using Co as a reference standard. As previously reported (e.g., Buchs et al. 2018a, b), the composition of augite standard NMNH 122142 analysed at Cardiff University by this method has a relative error generally < 10%, specifically ~1% for Si, Fe, Mg and Ca, ~6% for Al, ~10% for Na, ~20% for Ti, and ~30% for Cr (close to its detection limit of ~0.10 wt.%). Therefore, errors in SEM EDS analysis are significantly lower than the natural variability expected in our samples.

### Microprobe analysis

Microprobe analysis was performed at University of Bristol using a Cameca SX100 microprobe and a JEOL JXA8530F hyperprobe. Measurements were performed at 20 kV on the

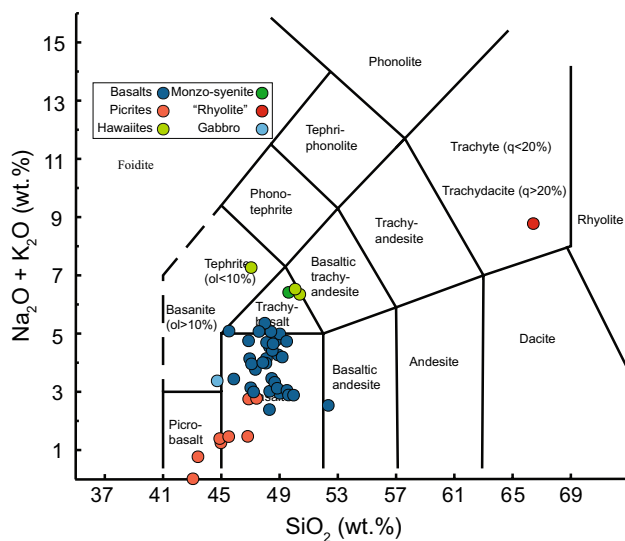


**Fig. 2** Total alkali-silica (TAS) diagram of the collection of whole rocks collected by Buchs et al. (2020) on a volatile-free basis, normalized to 100%, after Le Bas et al. (1986). Gabbro and monzosyenite compositions are included into the basalt and hawaiiite groups for the remainder of the discussion, respectively. The singular rhyolite sample is excluded from further discussion

Cameca system and 15 kV on the JEOL. Both systems operated at 40 nA, with a beam size set to 1  $\mu\text{m}$ . Secondary calibration was performed on labradorite, kaersutite, diopside, and Cr-spinel (SX100 only). Comparison with LA-ICP-MS results indicate that clinopyroxene (Cpx) Cr values from these analyses may be systematically underestimated (45–50% of LA-ICP-MS results) and are, therefore, considered with caution. However, based on secondary standardization, this may instead reflect interference in the LA-ICP-MS system (e.g.,  $^{40}\text{Ar}^{12}\text{C}$  and  $^{52}\text{Cr}$ ). Secondary calibration indicates that relative errors for major element concentrations in pyroxenes are generally  $<5\%$ :  $\sim 0.5\%$  for Mg,  $<2\%$  for Ca, 15% for Ti (at near-detection limit concentrations),  $\sim 13\%$  for Na, and  $\sim 2\%$  for Cr (at high concentrations in Cr-spinel). Microprobe and SEM EDS measurements were compared directly by duplicate analyses of 9 cpx crystals of variable compositions. These measurements were found to be consistent for most measured elements with, a mean relative error of 0.6% for  $\text{SiO}_2$ , 3.9% for  $\text{Al}_2\text{O}_3$ , and 9.4% for  $\text{Na}_2\text{O}$ . The mean relative error reached 21% for  $\text{Cr}_2\text{O}_3$  due to SEM EDS limitation at low elemental concentration. Cationic abundances were determined for cpx on a four cation, six oxygen basis, taking into account  $\text{Fe}^{3+}$  in the M1 site (Cameron and Papike 1981; Morimoto 1988; Stone and Niu 2009).

### LA-ICP-MS

LA-ICP-MS analysis was performed at Utrecht University using a ThermoFischer Scientific Element 2 magnetic sector

ICP-MS and a GeoLas 200Q Excimer laser ablation system (wavelength of 193 nm). Analyses used a beam diameter of 40–60  $\mu\text{m}$ , and a pulse repetition rate of 10 Hz and an energy density of 10  $\text{J cm}^{-2}$ . Data were acquired with 60 s of ablation, preceded and followed by gas background measurements. External calibration was carried out against glass reference material NIST SRM 612. Instrument performance and stability were monitored by measurement of USGS reference glass BCR-2G as a secondary standard throughout the procedure (Supplementary Materials 3). Based on these measurements, relative errors for analysis are  $<10\%$  for concentrations above 6 ppm,  $<15\%$  under 6 ppm, and  $<20\%$  under 1.2 ppm, with the exception of Pb ( $\leq 17\%$  at 11 ppm). CaO wt.% data from microprobe analyses were used as internal standard.

### Rhyolite-MELTS modelling

Major element modelling was performed using rhyolite-MELTS versions 1.0.2 (for anhydrous conditions) and 1.2.0 (for hydrous conditions) (Gualda et al. 2012) to characterise compositional changes associated with magmatic differentiation and help constrain approximate P–T conditions of crystallization of the studied transitional tholeiitic to alkaline magmatic suites. All runs were performed using an FMQ redox buffer, and primarily concerned anhydrous compositions, with a single exception. These assumptions are in agreement with the lack of primary hydrous phases in the studied igneous suites (Buchs et al. 2011; Gazel et al. 2018; this study) as well as redox conditions in other Pacific ocean islands (e.g., Geist et al. 1998; Brounce et al. 2017). We consider the potential for cryptic amphibole crystallization to be minor, based on cpx trace element compositions (see section on clinopyroxene trace element variability), ruling out significant hydrous influence on fractionation processes. As explained below, the studied picrites are porphyritic igneous rocks with significant olivine accumulation, and most basalts have undergone significant degrees of olivine fractionation. Therefore, an initial estimate for the starting composition was based on removal of primitive olivine and cpx from whole-rock (WR) compositions of picrites to obtain an approximate matrix ( $\sim$  melt) composition. These matrices, as well as chemically similar whole rocks, were then used as potential starting compositions. The olivine composition used in the matrix calculations is the most Fo-rich composition (AZ14-38S, Fo = 90.38) reported by Gazel et al. (2018). For cpx, we used the most primitive composition reported in this study (DB05-010 px 5, Mg# = 86.7; Supplementary Materials 3). The volume of phenocrysts removed for each picrite was based on manual selection on thin section images and volume calculation using Fiji by ImageJ software (Schindelin et al. 2012, 2015). Afterwards, whole-rock oxide concentrations were re-normalized to exclude

the phenocrystic component. We used a density of 3.2, 3.3, 3.4, and 2.75 g/cm<sup>3</sup> for whole-rocks, olivine (ol), cpx, and plagioclase, respectively.

## Cpx-liquid equilibrium test and geothermobarometry

### Major element equilibrium evaluations

Geothermobarometric calculations using the microprobe cpx dataset were performed using an approach adapted from Neave and Putirka (2017) and Neave et al. (2019). Cpx-WR pairs were determined on the basis of best-fit equilibrium calculations, in which equilibrium between cpx and picrite (adjusted for accumulation), basalt, and hawaiite whole-rock compositions (Buchs et al. 2011; this study for PA14-032, Supplementary Materials 2, 3) was tested in terms of Mg#, the structural components in the cpx, and the Ti-partition coefficient ( $D_{Ti}$ ). The  $Fe^{2+}/Fe^{3+}$  ratios in whole-rock data used to determine the  $K_D(Fe-Mg)^{cpx-liq}$  were determined by the approach of Kress and Carmichael (1991) assuming oxygen fugacity buffered to the quartz-fayalite-magnetite buffer at a temperature estimated using Eq. 14 of Putirka (2008). Picrite WR data uncorrected for olivine accumulation were not considered to represent potential carrier liquids because of high abundance of inherited olivine phenocrysts in these rocks (see below). To start, temperatures and pressures of crystallization were determined for every possible WR-cpx pair using Eq. 33 from Putirka (2008), and the  $Jd$ -in barometer from Neave and Putirka (2017), respectively. These equations are subject to SEEs of 45 °C and 1.4 kbar, respectively. We estimate equilibrium for each pair first by calculating the  $K_D(Fe-Mg)^{cpx-liq}$  value using Eq. 35 of Putirka (2008), with a temperature input in accordance with Eq. 33 of the same study. We assumed that cpx-liquid Mg# equilibrium was reached when the measured  $K_D(Fe-Mg)^{cpx-liq}$  of a given cpx-liquid pair fell within a 0.03 envelope (arbitrary value identical to Neave et al. (2019) chosen to be within sensible accuracy) of the value calculated based on the whole-rock composition. Diopside-Hedenbergite (DiHd), Enstatite-Ferrosilite (EnFs), and Calcium-Tschermak (CaTs) component equilibria were subsequently tested for each cpx-WR pair using the empirical approaches of Mollo et al. (2013a) (for DiHd, EnFs) and Putirka (1999) (for CaTs), using temperature and pressure inputs from the geothermobarometric calculations. Pairs were deemed in equilibrium with a whole-rock composition when measured components were within a threshold value of calculated values. We used thresholds of 0.06, 0.05, and 0.03 for the DiHd, EnFs, and CaTs components, respectively, corresponding to the standard estimated errors (SEE) reported by Mollo et al. (2013a) for their calibrated dataset, as well as those reported by Putirka (1999). Lastly, crystal-melt pairs were checked for Ti-equilibrium

using the approach by Hill et al. (2011) adjusted for the erratum of Hill et al. (2012). By use of this lattice strain parameterization model we calculated the appropriate Ti-partition coefficient for each cpx crystal, with which an equilibrium carrier equilibrium carrier liquid  $TiO_2$  concentration was calculated and compared with the matched whole-rock, using a moderately high equilibrium threshold  $TiO_2$  value of 2 wt.% (50–100% of whole rock concentrations). Only cpx-WR pairs which present equilibrium in terms of all tested parameters are considered to report petrologically meaningful P–T conditions. Cpx compositions which were found to be in equilibrium with multiple whole rocks have a range of temperatures and pressures reported. For comparison and due to the more alkaline compositions included in our dataset (hawaiites), the same approach was performed instead using barometric model P1 of Putirka et al. (1996) ( $SEE = 1.22$  kbar), in combination with the T2 thermometry model ( $SEE = 34$  K) of the same study. However, due to this barometer's systematic overestimation at low pressures (< 10 kbar) (Neave and Putirka, 2017), calculated pressures under 10 kbar were systematically adjusted. For the adjustment approach, a maximum overestimation of 3 kbar (at a calculated value of 2 kbar) was used, decreasing to an adjustment of 0 kbar for calculated values of 10 kbar. Sub-zero calculated pressures were subsequently discarded.

### Trace element modelling of carrier melts

Clinopyroxene-liquid rare earth element (REE) equilibria were modelled using the Lattice Strain Model approach of Wood and Blundy (1997) for all cpx-whole-rock pairs consistent with equilibrium in terms of Mg# and cpx-components. Because all considered pairs were in major element equilibrium, the pressures and temperatures required to determine cpx-melt REE partition coefficients were based on our geothermobarometric results as discussed previously. For each element and each pairing, expected cpx/melt partition coefficients ( $D$  or  $D_i$  for element  $i$ ) were calculated using Eq. 10 of Wood and Blundy (1997) at the pressure, temperature, and bulk chemical constraints of the pairing. Parameters  $r_0$ ,  $E_0$ , and  $D_0$  were calculated using Eqs. (15), (14), and (34) of Wood and Blundy (1997), using structural units as calculated on a 6-oxygen basis (see section on microprobe analysis), pressures and temperatures as calculated for major element equilibration, and the Mg# of the paired whole-rock. All calculations were performed once for the exact calculated pressure and temperature conditions, once for the lower estimates of both (-1SEE), and once for the upper estimate (+1SEE) values. The calculated partition coefficients were then compared to those observed in the cpx-WR pair based on ICP-MS analysis. As further explained below, we considered equilibrium to have been achieved when a majority of calculated values were within 20% of the measured partition

coefficients. Though pairs are still evaluated on an individual basis, this threshold was chosen to account for error propagation from trace element analyses and is not petrologically meaningful, especially given the increased errors in analysis on select trace elements (low vs high concentrations, paired vs unpaired electrons). Due to their different calibration sets, the cpx-WR matches and pressure–temperature conditions of the Neave and Putirka (2017) geothermobarometric approach are used for tholeiitic shield phase cpx, whereas those of Putirka et al. (1996) are used for alkaline post-shield phase cpx.

## Results

### Petrography and mineral composition

#### Whole-rock textures

The studied basalts possess an ophitic to microporphyritic texture dominated by cpx in a microcrystalline plagioclase matrix. No clear foliation is observed. Basalt sample DB06-084 (Supplementary Materials 1, Fig. S2b, S3) is moderately altered, reflected by widespread secondary mineralization in amygdales and chloritization of melt pockets, whereas DB07-013 and DB06-077 (Supplementary Materials 1, Fig. S3-4) appear fresh.

Hawaiite samples PA14-032 and DB06-007 are porphyritic, with phenocrysts of up to 3 mm in diameter, and a total crystal volume of 14–19% (Supplementary Materials 1, Fig. S2e, S6-7). Clinopyroxene and plagioclase feldspar are the dominant phenocryst phases. All phenocrysts are euhedral to subhedral with frequent resorption features in cores and/or rims (Supplementary Materials 1, Fig. S2e, S6-7). Amygdales in these rocks are scarce (<5%) and filled with secondary oxides and carbonates. The matrix is cryptocrystalline and dominated by laths of cpx and plagioclase feldspar (up to 90%), forming a weak magmatic foliation, with subordinate opaque oxides and infrequent alkali feldspar. Hawaiite DB07-021 has a texture similar to that of the other hawaiites but with slightly more pronounced subophitic character (Supplementary Materials 1, Fig. S2f, S8).

Picrites can be subdivided into three textural categories (Supplementary Materials 1, Fig. S2a, c, e, S9-12): olivine-dominated (DB05-010, DB07-024), glomeroporphyritic (DB06-038), and mixed (DB06-086). Olivine-dominated samples (Supplementary Materials 1, Fig. S2a, S9, S12) are highly porphyritic with a crystal volume up to 50%, comprised almost exclusively of olivine ( $\geq 50\%$  of crystals) and cpx (30–50%) with subordinate plagioclase. This type of picrite is often heavily altered, as evidenced by abundant serpentinization of olivine. The matrix is composed primarily of cpx and minor plagioclase feldspar within an altered

glass matrix. Glomeroporphyritic picrite DB06-038 (Supplementary Materials 1, Fig. S2c, S10) has a crystal content of  $\sim 60\%$  (25% olivine, 25% cpx, 10% plagioclase). Both olivine and cpx form glomeroporphyritic complexes within a matrix of moderately altered glass. Mixed picrite DB06-086 (Supplementary Materials 1, Fig. S2e, S11) has 30% of its crystal population composed of sub-equal proportions of olivine, cpx, and plagioclase. Clinopyroxene phenocrysts are either subhedral or anhedral and resorbed, whereas olivine is exclusively anhedral, and feldspars are euhedral to subhedral. The matrix of this sample is cryptocrystalline with abundant plagioclase laths and cpx and no clear foliation.

#### Olivine

Olivine was only found in picrite samples. Crystals ( $\leq 5$  mm diameter) are rounded, fractured, and frequently altered to serpentine (Supplementary Materials 1, Fig. S13a). Geochemical analysis of olivine was beyond the scope of our study that focused on pyroxenes. Where olivine compositions were needed, we used the dataset of Gazel et al. (2018), who focused on the geochemistry of olivine in the same magmatic series.

#### Plagioclase

Plagioclase is present in all samples as groundmass, phenocryst, and inclusions in cpx (Fig. 3f;). Phenocrysts are subhedral to anhedral with oscillatory zoning. Resorbed cores are common in hawaiite DB06-007 (Supplementary Materials 1, Fig. S13b,c). Plagioclase inclusions in cpx from hawaiites are circular and up to 200  $\mu\text{m}$  in diameter, whereas those in cpx from picrite DB06-086 are best described as subhedral chadacrysts (early-formed crystals enclosed by later crystallizing phases) of up to 2 mm in diameter (Fig. 3f).

#### Clinopyroxene

All studied samples contain cpx of augite to diopside composition (Table 1), which can be subdivided into five populations, termed here M-, R1-, R2-, H-, and S-type, based on chemical and morphological characteristics (Fig. 3; Table 1). M-type cpx are microphenocrysts found in all basalt samples (Supplementary Materials 1, Fig. S2, S3-5; Fig. 3a). These cpx are  $< 400$   $\mu\text{m}$  in diameter and can be distinguished by their euhedral habit and micron-scale oscillatory zoning (Fig. 3a). R1-type cpx are well-rounded phenocrysts found exclusively in picrites. These phenocrysts have diameters of up to 4 mm, and frequently have magnesium-rich ( $\text{Mg}\# = 82\text{--}87$ ) cores surrounded by a more evolved rim ( $\text{Mg}\# = 73\text{--}79$ ) rim (Fig. 3b,c). Cr-spinel is a common inclusion phase in this crystal-type

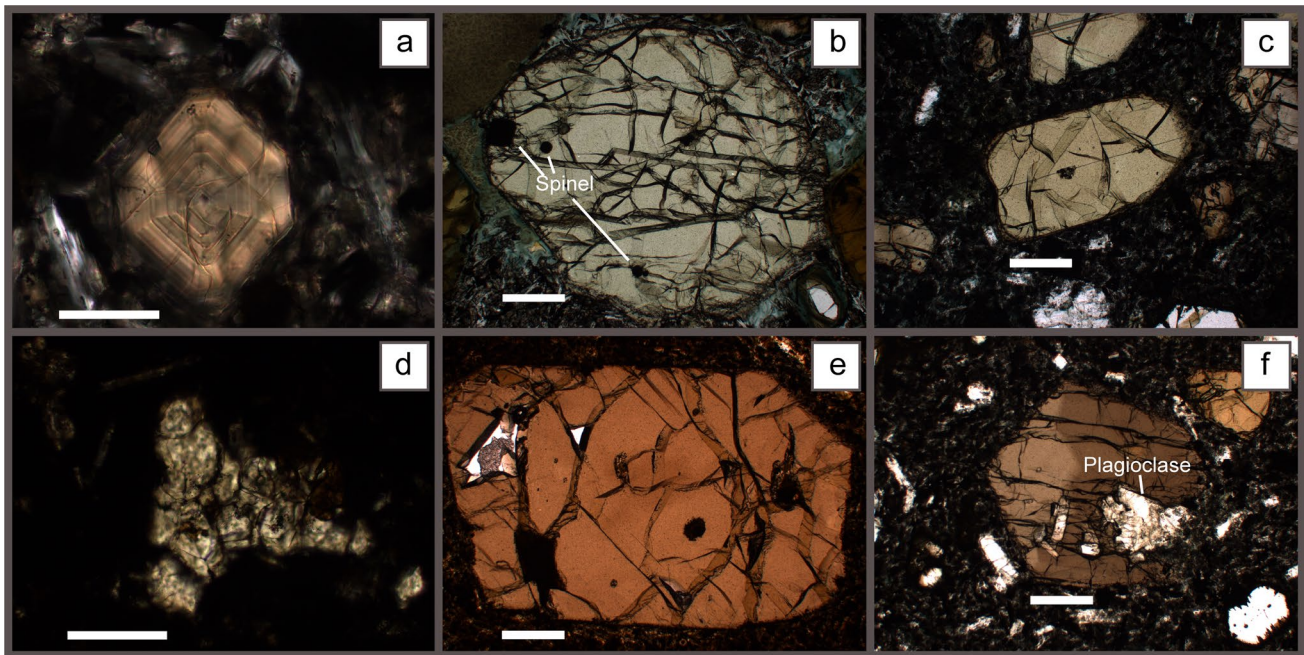


**Fig. 3** OM images of different morphological cpx types under plane polarized light. **a** M-type from DB06-077 [scale bar 50  $\mu\text{m}$ ], **b** R1 phenocryst from DB05-010 as also found in DB07-024 (cpx 5) [scale bar 500  $\mu\text{m}$ ]; black inclusions are spinel, **c** R1 phenocryst from DB06-086 [scale bar 500  $\mu\text{m}$ ], **d** Aggregate of R2-type phenocrysts

from DB07-013 (cpx 1) [scale bar 200  $\mu\text{m}$ ], **e** H-type phenocryst from PA14-032, Ti-richness is exemplified by red colour (cpx 1) [scale bar 500  $\mu\text{m}$ ], **f** S-type phenocryst (086 cpx 4) with a Ti-rich (right) and Ti-poor (left) zone [scale bar 500  $\mu\text{m}$ ], white chadacrysts are plagioclase feldspar

(Fig. 3b), in line with this being the most Mg-rich population in the magmatic series. R2-type cpx are another variety of rounded phenocrysts found in all basalt samples, as well as picrite DB06-038. R2-type cpx consist of anhedral crystals of up to 400  $\mu\text{m}$  without internal zoning, occurring as isolated crystals and/or monomineralic glomerocrysts (Supplementary Materials 1, Fig. S2c; Fig. 3d). Though not as primitive in composition as R1-types, this is the second most Mg-rich crystal population (Table 1). H-type cpx are found exclusively in hawaiite samples DB06-007 and PA14-032 and represent the most Mg-poor, evolved cpx population. These cpx have diameters between 0.5 and 5 mm, are Ti-rich ( $\text{TiO}_2 = 1.3\text{--}3.3$  wt.%, median =  $2.4 \pm 0.3$  ( $1\sigma$ ,  $n = 126$ ); Table 1) and chemically homogeneous, with an intense reddish/brownish colour in thin section (Fig. 3e). S-type cpx are sector zoned crystals found exclusively in picrite sample DB06-086. They have multiple chemical zones (or sector zones; Fig. 3f) that correspond to Ti-rich ( $\text{TiO}_2 = 1.7\text{--}2.4$  wt.%) and Ti-poor ( $\text{TiO}_2 = 1.3\text{--}1.6$  wt.%) compositional end-members (Table 1). S-type cpx commonly host plagioclase chadacrysts (Fig. 3f). Detailed chemical characteristics of the five cpx types are discussed in the clinopyroxene geochemistry section and can be found in Supplementary Materials 2.

### Magmatic differentiation of carrier liquids

The Hoya Island picrites, basalts, and hawaiites form three distinct populations in terms of bulk rock chemistry (Fig. 4, 5), which appear primarily separated by Mg# and alkali content. The hawaiites (including the single monzosyenite sample) represent the most evolved magmas (of the post-shield alkaline phase) with Mg# = 30–42 and a lower CaO content, but higher  $\text{Al}_2\text{O}_3$  relative to the more magnesian basalts. The hawaiite  $\text{TiO}_2$  content is similar to basalt samples with Mg# of  $\sim 50$ , indicating a relative depletion for their Mg content. The bulk of the basalts (including the single gabbro sample) have Mg# ranging between 40 and 58, the most Mg-rich sample being DB06-134 (Mg# = 58.6).  $\text{TiO}_2$  and  $\text{Al}_2\text{O}_3$  decrease with Mg# from 4.3 to 2.7 wt.% and 15.2 to 13.4 wt.%, respectively (Fig. 4b, c). In contrast, CaO decreases with differentiation from 11.6 to 8.9 wt.%, albeit with significant scatter, and  $\text{SiO}_2$  follows a convex pattern with Mg# between 46.9 and 48.9 wt.%, peaking at Mg# = 49.7 with 50 wt.%. The picrites form a compositional trend between high-Mg# basalt and pure olivine compositions. This feature, in combination with the highly porphyritic texture of the picrites and resorption of some of their olivine phenocrysts, suggests that olivine accumulation in basaltic melts controlled the formation of the picrites

**Table 1** Representative cpx analyses of all morphological and chemical groups per thin section in which they occur

Sample	PA14-32	DB06-007	DB06-084	DB06-084	DB06-086	DB06-086	DB06-086	DB07-013	DB07-013	DB05-010
Crystal	3	1	5	2	12	10	10	6	9	1
Type	H	H	R2	M	R1	S (High-Ti)	S (Low-Ti)	R2	M	R1
SiO <sub>2</sub>	48.53	48.48	50.53	49.61	49.94	49.24	50.90	51.34	49.34	50.56
TiO <sub>2</sub>	2.38	2.24	1.36	1.39	1.30	1.95	1.36	1.05	1.83	0.95
Al <sub>2</sub> O <sub>3</sub>	5.48	5.36	3.95	5.02	4.25	4.31	3.01	3.41	4.66	4.18
Cr <sub>2</sub> O <sub>3</sub>	0.09	0.18	0.42	0.75	0.96	0.19	0.14	0.56	0.08	1.15
FeO	7.30	7.43	6.66	6.61	5.27	7.87	7.69	6.20	9.07	4.99
MnO	0.11	0.11	0.14	0.12	0.11	0.17	0.18	0.14	0.18	0.09
MgO	13.63	13.82	15.51	14.98	15.53	14.23	15.31	16.14	14.96	15.71
CaO	22.19	22.06	21.31	21.27	21.82	21.53	21.05	21.07	19.68	22.19
Na <sub>2</sub> O	0.45	0.48	0.29	0.26	0.32	0.35	0.37	0.28	0.32	0.28
K <sub>2</sub> O	<0.01	<0.01	<0.01	<0.01	<0.01	<0.01	<0.01	<0.01	0.01	<0.01
Total	100.17	100.16	100.17	100.03	99.50	99.84	100.01	100.21	100.13	100.09
Si	1.80	1.79	1.86	1.83	1.84	1.83	1.88	1.88	1.83	1.85
Ti	0.07	0.06	0.04	0.04	0.04	0.05	0.04	0.03	0.05	0.03
Al (T)	0.20	0.21	0.14	0.17	0.16	0.17	0.12	0.12	0.17	0.15
Al (M1)	0.04	0.03	0.03	0.05	0.03	0.02	0.01	0.03	0.03	0.03
Cr <sup>3+</sup>	0.00	0.01	0.01	0.02	0.03	0.01	0.00	0.02	0.00	0.03
Fe <sup>3+</sup>	0.06	0.08	0.04	0.04	0.05	0.06	0.05	0.03	0.06	0.05
Fe <sup>2+</sup>	0.16	0.15	0.16	0.16	0.11	0.18	0.18	0.16	0.22	0.11
Mn	0.00	0.00	0.00	0.00	0.00	0.01	0.01	0.00	0.01	0.00
Mg	0.75	0.76	0.85	0.82	0.85	0.79	0.84	0.88	0.83	0.86
Ca	0.88	0.87	0.84	0.84	0.86	0.86	0.83	0.83	0.78	0.87
Na	0.03	0.03	0.02	0.02	0.02	0.03	0.03	0.02	0.02	0.02
K	0.00	0.00	0.00	0.00	0.00	0.00	0.00	0.00	0.00	0.00
Wollastonite	47.3	46.8	44.2	44.9	45.8	45.2	43.4	43.4	41.2	46.2
Enstatite	40.4	40.8	44.8	44.0	45.4	41.6	43.9	46.3	43.6	45.5
Ferrosilite	12.3	12.5	11.0	11.1	8.8	13.2	12.7	10.2	15.1	8.3

Cation proportions are calculated on a 6 oxygen basis taking into account Fe<sup>3+</sup> in the M1 site (Cameron and Papike, 1981; Morimoto, 1988; Stone and Niu, 2009). Ferric iron calculated using approach of Lindsley (1983). Pyroxene components wollastonite, enstatite, and ferrosilite are noted in percentages

during the transitional tholeiitic shield phase of the island. Picrite formation by mineral accumulation in a transitional tholeiitic basaltic melts is also consistent with crystal-liquid disequilibrium of both cpx (see below) and olivine (Gazel et al. 2018), and with the basaltic composition of the matrix of three picrites, as estimated by subtracting phenocrysts chemistries from bulk-rock data. Nevertheless, the matrix of picrite DB05-010 has a distinctly higher Mg# (70.8) than Hoya basalts and other calculated picrite matrices, which suggests that the composition of this matrix may lie close to that of a parental melt for the transitional tholeiitic series of the shield volcanic stage of the island. This is consistent with the composition of cpx phenocrysts in this sample having the highest Mg# of our dataset (see section on clinopyroxene geochemistry).

Rhyolite-MELTS modelling of the liquid lines of descent of the shield transitional tholeiitic (basaltic) and post-shield

alkaline (hawaiite) series was attempted using a variety of whole-rock compositions close in composition to the matrix of picrite DB05-010 (Mg# = 70.8; Supplementary Materials 2). The best result for the transitional tholeiitic series was found using equilibrium fractionation using unadjusted picrite sample DB07-014 as starting composition (Supplementary Materials 2) at pressures of 2–3 kbar and FMQ redox conditions (Chosen as approximation based on Cottrell et al. (2021) as well as the redox conditions in other Pacific ocean islands (e.g., Geist et al. 1998; Brounce et al. 2017)). This sample shows the least signs of olivine accumulation among picrites, and has a more appropriate Al<sub>2</sub>O<sub>3</sub> and CaO content than the DB05-010 matrix. It is not considered a primary liquid, but serves as an adequate parental melt composition. Rhyolite-MELTS modelling using the DB05-010 matrix composition produces trends too low in SiO<sub>2</sub> and displaced towards higher MgO, likely reflecting the enduring

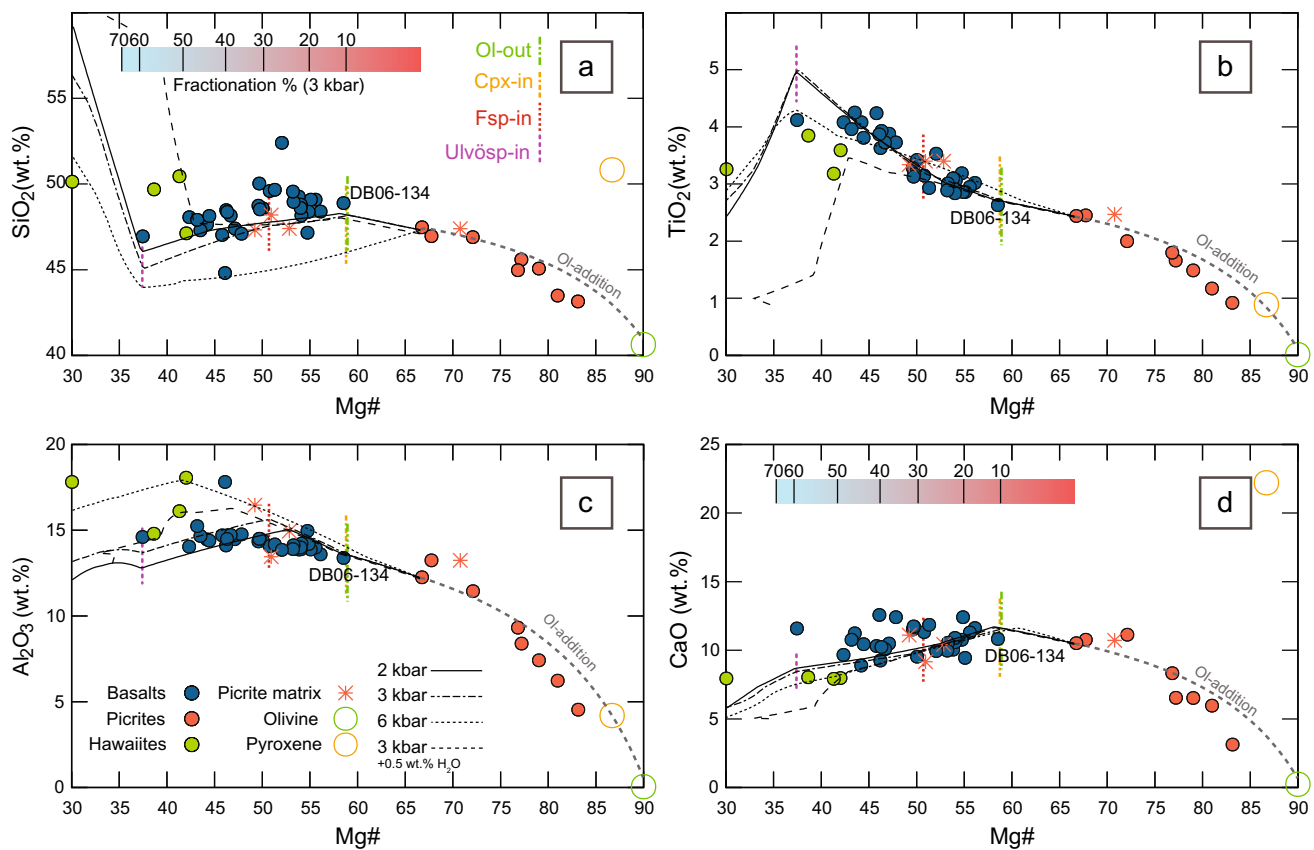


**Fig. 4** Harker diagrams for  $\text{Al}_2\text{O}_3$ ,  $\text{CaO}$ ,  $\text{TiO}_2$ , and  $\text{SiO}_2$ , versus  $\text{Mg}\#$ , functioning as a fractionation proxy. Whole-rock data are reported on a volatile-free basis and are normalized to 100%. Liquid lines of descent are listed for 2, 3, and 6 kbar melt fractionation from sample DB07-014, as well as 3 kbar fractionation with 0.5 wt.%  $\text{H}_2\text{O}$ . Liquid lines are based on rhyolite-MELTS modelling (Gualda et al. 2012) as discussed in the Materials and Methods section. Basalt sample

DB06-134 is highlighted as the most primitive tholeiitic basalt. Representative compositions of pyroxene and olivine are the most primitive reported analyses from this study and Gazel et al. (2018), respectively. Mineral-in and -out lines, as well as fractionation percentages are reported for 3 kbar anhydrous fractionation. Beyond DB07-014 we've included dashed lines indicative of olivine addition (olivine composition from Gazel et al. (2018))

effects of accumulation even after (inherently semi-quantitative) adjustment. Anhydrous, isobaric crystallization with decreasing temperature using composition DB07-014 at 2–3 kbar produced olivine, followed by Cr-spinel, cpx, plagioclase, ulvöspinel, magnetite, whitlockite, and ilmenite, resulting in better fitted liquid lines of descent (Fig. 4, 5). These models are additionally in general agreement with petrographic observations and reproduce the broad chemical trends of the transitional basalt series. Modelling at higher pressures ( $\geq 4$  kbar) instead cause an interval of early opx crystallization to be predicted, as well as delayed feldspar crystallization, which together cause  $\text{SiO}_2$  to be underestimated and  $\text{Al}_2\text{O}_3$  to be overestimated at these pressures. In a similar fashion, the addition of 0.5 wt.%  $\text{H}_2\text{O}$  to the 3 kbar model causes liquid lines to significantly underestimate estimate  $\text{TiO}_2$  concentrations, due to crystallization of more Ti-rich cpx and an overall delay in the crystallization of Ti-poor phases (Fig. 4b) These observations constrain differentiation conditions of the tholeiitic series to anhydrous

crystallization at 2–4 kbar. Note, however, that this model fails to reproduce the exact crystal compositions observed in picrites, which have a higher  $\text{Mg}\#$  still (85–86 vs the modelled 82). This discrepancy reflects later cpx crystallization than observed and a more dominant EnFs component in the modelled crystal compositions, as opposed to the more DiHd-rich natural samples (Supplementary Materials 1, Fig. S15, S16). Hawaiite compositions are approximately reproduced using equilibrium crystallization from the same parental liquid used for the transitional tholeiitic series at pressures close to 6 kbar (Fig. 4). Nevertheless,  $\text{SiO}_2$  concentrations are not satisfactorily reproduced. At this pressure, in contrasting to petrographical evidence, opx replaces olivine as the first crystallizing phase, after which the 2–3 kbar fractionation path is followed from spinel onwards. The three highest  $\text{Mg}\#$  hawaiite series rocks are additionally in good agreement with hydrous (0.5 wt.%  $\text{H}_2\text{O}$ ) fractionation at 3 kbar. Under these conditions, cpx and especially feldspar crystallization are delayed ( $\text{Mg}\#$  46.6 vs 50.7), and

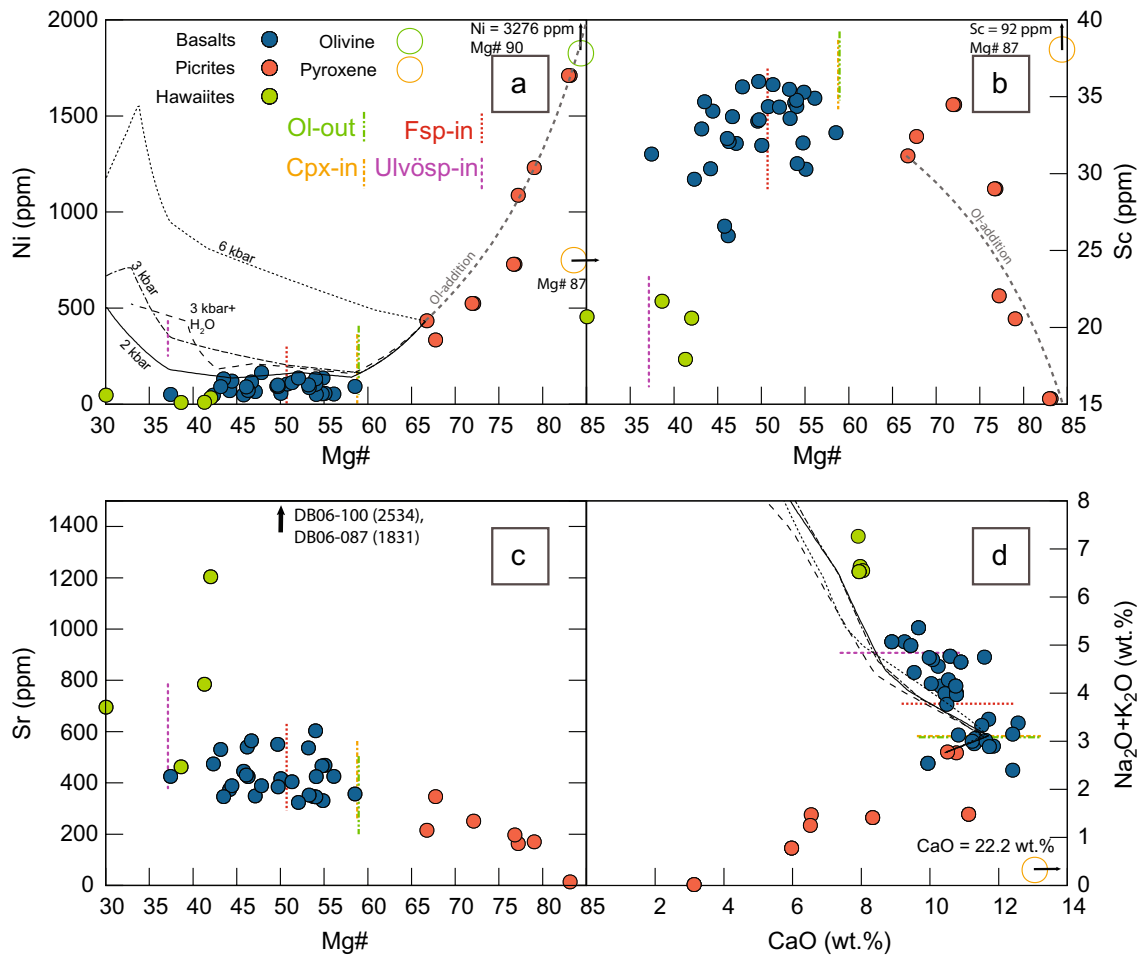


**Fig. 5** **a-c** Ni, Sc, and Sr vs Mg# diagrams for whole-rock compositions from Buchs et al. (2011) indicating degrees of olivine, pyroxene, and plagioclase crystallization during fractionation, respectively. **d** Alkali vs CaO diagram indicating a lack of positive correlation between alteration and CaO concentrations. Liquid lines are included

based on rhyolite-MELTS modelling (Gualda et al. 2012) as discussed in the Materials and Methods section. Olivine addition lines are included for Ni (**a**) and Sc (**b**), reflecting the fractionation/accumulation path represented by the picrites (olivine composition from Gazel et al. (2018))

whitlockite is replaced by apatite. Melt curves corresponding to hydrous fractionation are in better SiO<sub>2</sub> and TiO<sub>2</sub> agreement with the higher Mg# hawaiite samples, but disagree with sample DB06-007. However, there are too few hawaiite samples to rule out the possibility of anhydrous fractionation in the hawaiites based on rhyolite-MELTS curves.

Additional constraints on the role of olivine, cpx and plagioclase fractionation/accumulation (and possibly source composition) are provided by Ni, Sc and Sr, respectively, which are highly compatible in these phases. Ni and Sc both decrease with decreasing Mg# in the basalt + hawaiite series (Fig. 5). Ni decreases strongly from ~1750 to ~300 ppm with decreasing Mg# in picrites, but only moderately decreases from ~200 to ~0 ppm in basalts and hawaiites (Mg# < 60), forming an apparent differentiation/accumulation compositional continuum with the picrites (Fig. 5a). This trend is mirrored by Cr, which decreases significantly between

picrites (~1700 to ~700 ppm), but reaches a shallower slope for the basalts (~16 ppm per Mg#). Sc instead increases from ~15 to 35 ppm with decreasing Mg# in the picrites, then decreases steadily from ~35 to ~25 ppm in the basaltic interval as cpx starts to crystallize (Mg# = 60–40). The hawaiites have distinctly lower Sc (~20 ppm) than the transitional tholeiitic basalts, consistent with their differentiated character (Mg# = 30–42) and delayed plagioclase crystallization at higher pressure or higher water content in this alkaline series (Fig. 5b). Sr increases from ~0 to ~400 ppm with decreasing Mg# in the picrites, and from ~400 to ~500 ppm in the basalts (Fig. 5c). Two samples with unusually high Sr probably reflect alteration, but the lack of significant correlation between LOI and fluid mobile elements (Supplementary Materials 1, Fig. S1), together with highly consistent correlation between CaO and Na<sub>2</sub>O + K<sub>2</sub>O in the different rock types (Fig. 5d), suggest insignificant alteration effects

in most of the samples. Hawaiites have a more elevated Sr content than basalts (~750 ppm vs ~500 pm) at similar Mg# (Fig. 5c), which may reflect more extensive fractionation with cpx as the main crystallizing phase (as suggested by Sc), or a distinct magmatic source during post-shield magmatism. Perhaps more directly, the relative abundance of feldspar phenocrysts in the hawaiite samples (Supplementary Materials 1, Fig. S2d, S6, S7) may also have preferentially enriched the sample material in feldspar-compatible elements. The trends for Ni and Sc in basalts are in agreement with fractionation results from rhyolite-MELTS modelling at 3 kbar, indicating that olivine stops crystallizing when the melt Mg# reaches 59–60, and cpx starts to crystallize at Mg# = 59. However, the onset of plagioclase crystallization at Mg# = 51 predicted by rhyolite-MELTS modelling does not correspond to any clear change in Sr-Mg# trends. This discrepancy is supported by petrographic observations from high Mg# (> 55) basalts and picrites (e.g., DB07-013; DB06-038) which suggest that plagioclase crystallizes significantly earlier in the transitional tholeiitic sequence than in model predictions. The lower Sc and higher Sr signals in hawaiites are consistent with early pyroxene and late plagioclase crystallization predicted by rhyolite-MELTS modelling at 6 kbar, but the low Ni concentrations in the hawaiites argue for a larger window of early olivine crystallization instead of the window of opx crystallization predicted at these pressures. Nevertheless, no liquid lines with the current starting composition are able to reproduce the most Mg-rich R1-type clinopyroxene crystals (Mg# = 86.7) found in the picrites, which must have crystallized from a higher Mg# melt than current models predict for the onset of cpx crystallization.

### Clinopyroxene geochemistry

With the exception of M-type cpx, all cpx populations have a distinct geochemical signature, ranging from the primitive R1-type cpx hosted in picrites (Mg# = 80–87, excluding rims; Table 1), to the H-type cpx hosted in hawaiites (Mg# = 69–77; Table 1), which have a more significant jadeite-component (Table 1). S-type cpx have bimodal high- $(\text{TiO}_2 = 1.73\text{--}2.44 \text{ wt.}\%)$  and low-Ti  $(\text{TiO}_2 = 1.30\text{--}1.61 \text{ wt.}\%)$  compositions that correlate to the observed sector zoning, covering an Mg# range of 71–78 and 75–79, respectively (Table 1). (for a complete overview, see Supplementary Materials 3). M-type microphenocrytic cpx from basalts DB07-013 and DB06-084 cover the largest compositional range of all analysed cpx types, encompassing compositions of all other types except for R1. Together with their very distinctive micro-oscillatory zoning (Supplementary Materials 1, Fig. S14), this suggests step wise crystallization in a variety of conditions/melts.

Representative element maps (Fig. 6a) of the studied cpx phenocrysts clearly outline the high chemical variability in M-type cpx (Fig. 6a), as well as the stark chemical contrast between individual zones within S-type pyroxenes (Fig. 6b). Individual growth zones of M-type crystals are up to 20 microns wide (Fig. 6a); and may exhibit hourglass zoning. In the simplest sense, the oscillatory growth zones represent alternating rims of more primitive (Mg- and Cr-rich) and evolved (Mg- and Cr-poor) zones, both of which are equally affected by potential hourglass zoning (Fig. 6a). Element maps of S-type pyroxenes are in agreement with observations in optical microscopy (Fig. 3f; 6b). High-Ti signatures coincide with high concentrations of Al and low concentrations of Mg and Si (Fig. 6b). Cr is too low in concentration to accurately measure in element mapping, but electron probe measurements indicate this element to be enriched in high Ti zones (Fig. 6b). Whereas zoning in R1-type pyroxenes is mostly limited to normal zonation with a lower Mg# outer rim (Fig. 6c), more complex, multi-stage growth patterns can be discerned in a few crystals (Supplementary Materials 1, Fig. S14).

### Clinopyroxene trace element variability

All cpx types have similar Primitive Mantle (PM)-normalised trace element patterns (Fig. 7), with a generally concave downward shape and negative Sr and Zr anomalies, as commonly observed for cpx in transitional tholeiitic to alkaline series (e.g., Marks et al. 2004). Despite broad similarity, distinct overall trace element abundances can be observed in the different cpx types. R1-type cpx from picrite DB05-010 and R2-type cpx from basalt DB07-013 are the most depleted, chemically similar variants (Fig. 7d). R2-type cpx from basalt DB06-084 instead shows close overlap with basalt-hosted M-type cpx. This is in line with their lower Mg# compared to R2 from DB07-013, and indicates that R2-type cpx from different samples are chemically distinct in both major and trace elements. Nevertheless, a shallow slope towards HREE is shared between the R2-types from DB07-013 and M-types from DB06-084, reflected in comparatively low Dy/Yb (1.8–2.8) and Ti/Yb (5900–8700) ratios (Fig. 8a, b). As previously suggested, based on microprobe Ti results, the trace element contents of S-type cpx are strongly bimodal, with the highest trace element contents correlating to Ti-rich sectors. Despite Zr being depleted in all samples, this feature is most pronounced in R1- and R2-types from picrites and basalt samples, respectively. R1-types from DB05-010 are distinctly depleted in trace elements compared to those from DB06-086 (Fig. 7d), despite significant overlap in texture and major element compositions. The least variable trace element signal between crystals is found in H-type pyroxenes, which are more enriched in



**Fig. 6** EMPA measurement profiles matched with elemental mapping or BSE imagery of **a** M-, **b** S-, and **c** R1- type pyroxenes. M-type crystal 2 of DB06-084 is displayed in terms of a Cr-map, showing alternation of Cr-rich and Cr-poor zones. The profiled area is represented by a simplified sketch for clarity. Panel **b** shows an Mg-map of a sector zoned cpx in DB06-086 with a Ti-poor (left) and Ti-rich zone (right). The corresponding profile indicates the coupling of elements between sectors. Panel **c** displays a BSE image of an R1 type cpx of DB06-086, exemplified by its highly primitive core and much more evolved rim. Distances reported in profiles are measured from rim to core

LREE and slightly more depleted in HREE than M- and S-type cpx. Comparative depletion of HREE with respect to the cpx from transitional tholeiitic rocks is reflected in high Ti/Yb (9600–1300), Dy/Yb (2.8–3.8), and La/Sm (0.52–0.74) ratios (Fig. 8). Selected H-type pyroxenes additionally contain high  $Eu_N/Eu^*$  values (0.37–0.40) outside of the main array (0.28–0.34), potentially reflecting variable amounts of feldspar assimilation/dissolution during magma mixing (Fig. 8e). Progressive enrichment of Dy from R-types towards alkaline H-type pyroxene and a corresponding lack of variation in the Dy/Yb ratio

rules out cryptic amphibole formation during fractionation (Fig. 8d).

### Clinopyroxene geothermobarometry

Within the complete set of 821 cpx measurements, 602 (74%) were found to be in Mg#, DiHd, EnFs, CaTs,  $K_D(Fe-Mg)^{Cpx-liq}$ , and Ti-equilibrium with any of the transitional tholeiitic and alkaline whole-rock compositions from Hoya Island (Supplementary Materials 1, Fig. S15, 16; Supplementary Materials 3, Tables S2; S3). 129 measurements among the equilibrated pairs (15.7% of total) were found to be in equilibrium with their host rock, all of which were M- or R2-types derived from basalt samples DB06-084 and DB07-013. Identical modelling using the geothermobarometric equations of Putirka (1996) instead results in 365 measurements in equilibrium with a whole-rock composition (44%), 41 (5% of total) among which are equilibrated with their host. These last measurements were again primarily M- and R2-types from the tholeiitic basalts. In total, this amounts to 3432 equilibrium pairs following the equations of Neave and Putirka (2017) and 2148 pairs following Putirka et al. (1996)'s equations. A complete distribution

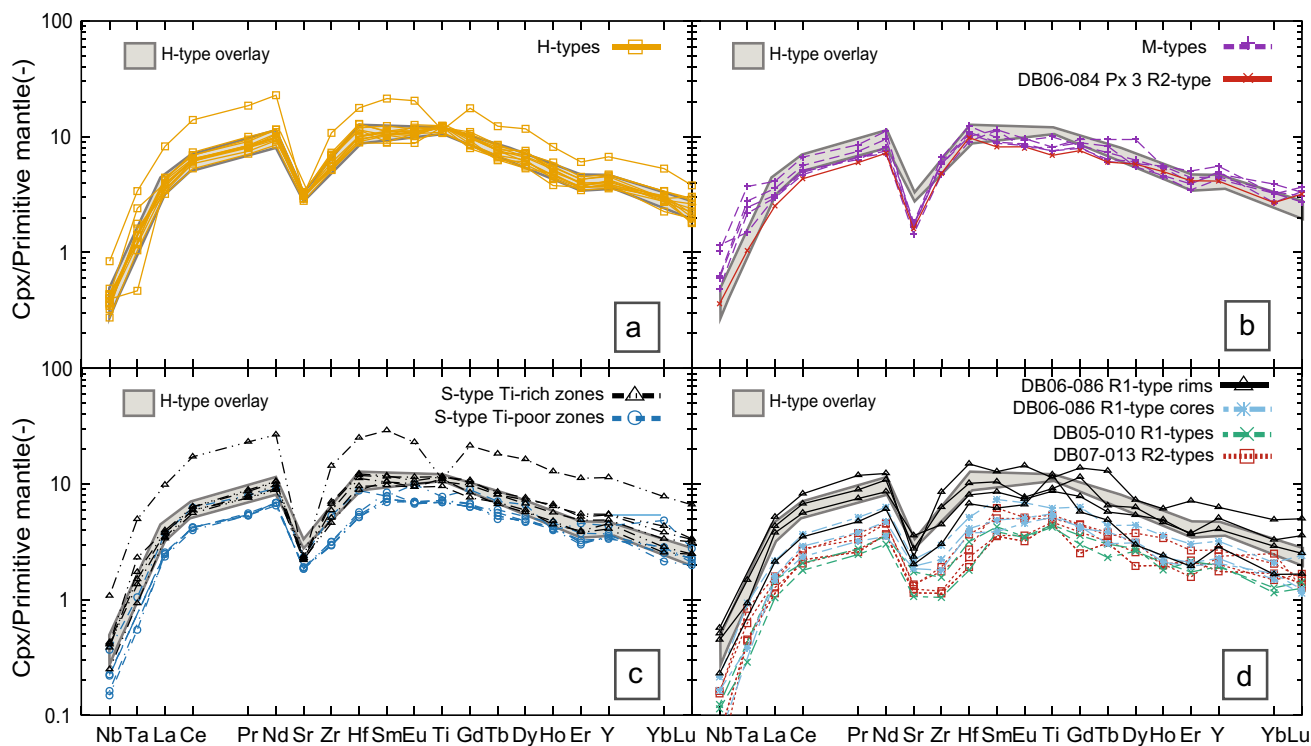


**Fig. 7** Trace element variability diagrams for the different pyroxene types, as measured by LA-ICPMS. Element order from incompatible to compatible in cpx, normalized to primitive mantle values from McDonough and Sun (1995). Hawaiite background shading is introduced in all diagrams as representative of hawaiite-type cpx composition (panel (a)). Sector zoned cpx (c) are displayed per sector,

showing the enrichment of trace elements in Ti-rich zones. R2 types of DB06-084 are in closer in trace chemical composition to M-type cpx and are therefore included in panel (b), whereas DB07-013's R2 types are chemically more comparable to R1-type cpx displayed in panel (d)

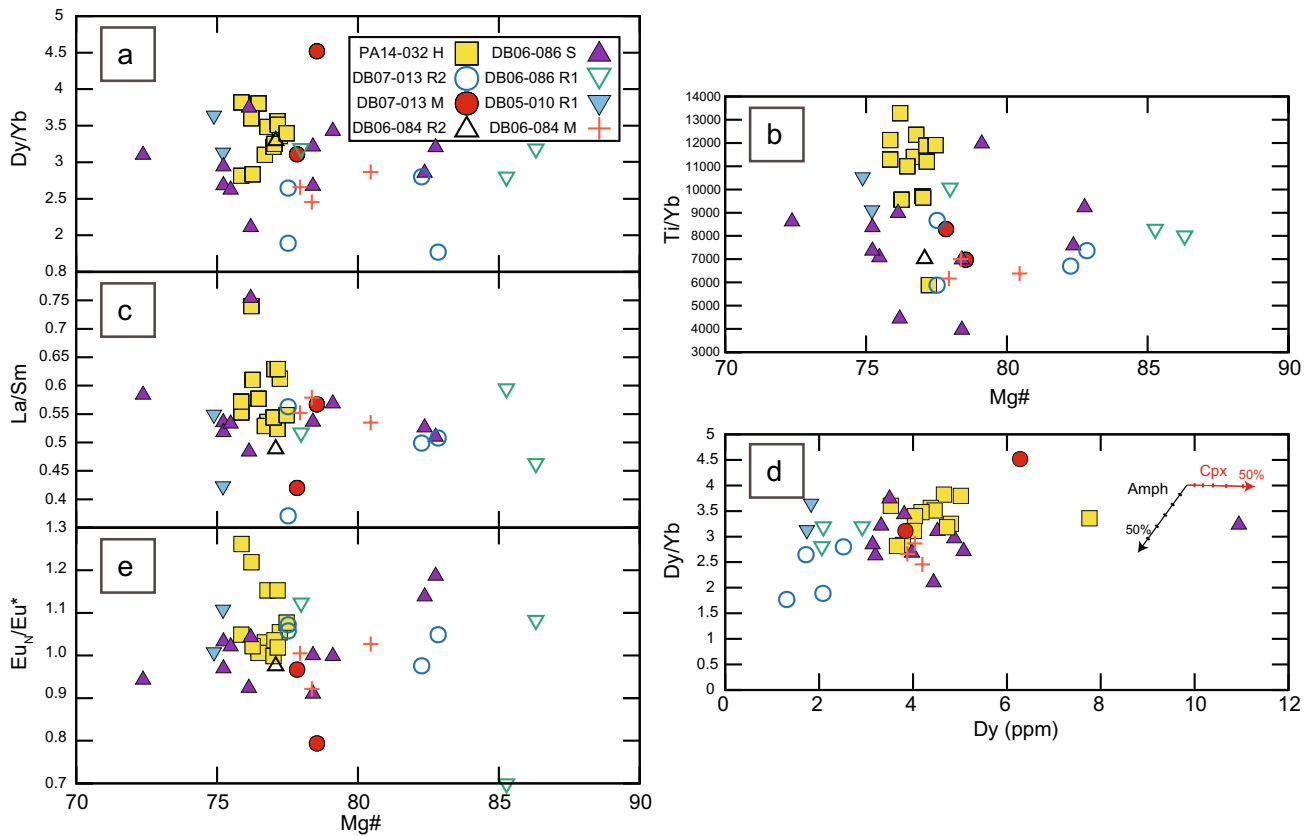


**Fig. 8** Cpx trace elements and ratios for each crystal type. Titanium and Mg# data are from associated microprobe data.  $Eu/Eu^*$  represents the Eu-anomaly and is defined as  $Eu_N/(Sm_N * Gd_N)^{1/2}$ . Amph-

bole and clinopyroxene fractionation lines as shown in panel (d) are adapted from Wang et al. (2019) and indicate a lack of influence of amphibole crystallization

of equilibrium pairs per whole-rock can be found in Supplementary Materials 3, in the form of Tables S2 and S3. In the following text, the Neave and Putirka (2017) model will be primarily discussed, given that it is preferred for all but the H-type cpx. Due to the nature of the whole-rock dataset, crystals with intermediate compositions (in terms of Mg#, such as M- and R2-types) were found to be in equilibrium with a larger amount of potential carrier liquids. M-type cpx WR matches are particularly diverse, with 24 (DB06-084) to 28 (DB07-013) liquids all representing > 1% of the matches. In contrast, we find R1-type cpx to be primarily equilibrated with a select group of the most Mg-rich compositions (e.g., 74% of the 133 R1-pairs of DB06-084) to 28 (DB07-013) liquids all representing > 1% of the matches. In contrast, we find R1-type cpx to be primarily equilibrated with a select group of the most Mg-rich compositions (e.g., 74% of the 133 R1-pairs of DB06-084) to 28 (DB07-013) liquids all representing > 1% of the matches. It is worth noting that these matches only represent 84 out of 199 R1-type measurements, which exclude the most Mg-rich compositions ( $Mg\# > 85.4$ ) for which DB06-134 is not primitive enough. In addition, no matches were found with the matrix of DB05-010 ( $Mg\# = 71.3$ ), indicating that their equilibrium melt is most likely compositionally intermediate between that sample and basalt DB06-134. R2-type crystal pairs are similarly limited to higher Mg# (> 50) melts, but to a lesser

degree. A moderate amount of H-type cpx-WR equilibrium pairs can be found when using the Neave and Putirka (2017) model, most of which match with DB06-083, a transitional basalt with  $Mg\# 50.4$ . When using the Putirka et al. (1996) model, however, an unimpressive seven measurements find equilibrium compositions, all of which are significantly closer to hawaiiite composition ( $44.5 < Mg\#$ ). Given that the Neave and Putirka (2017) model is not calibrated for alkali-rich compositions, the results of the model of Putirka et al. (1996) are nevertheless judged more likely to be petrologically realistic. In line with their compositional sectors, the S-type cpx equilibrium liquids are bimodally distributed between a Mg-rich ( $Mg\# 50.4$ – $51.7$  for low-Ti zones) and Mg-poor ( $Mg\# 44.5$ – $47.5$  for high-Ti zones) group.

P–T conditions of crystallization obtained from the Neave and Putirka (2017) cpx-melt pairs considered to be in major element equilibrium form three arrays: a high pressure ( $5.3 \pm 0.7$  kbar) group formed by H-type cpx in the hawaiites of the post-shield phase, a low-temperature ( $1146 \pm 17.3$  °C) group of S-type crystals divided between high (high-Ti sectors;  $4.2 \pm 0.8$  kbar) and low pressures (low-Ti sectors;  $2.6 \pm 1.4$  kbar), and a major array of R1-

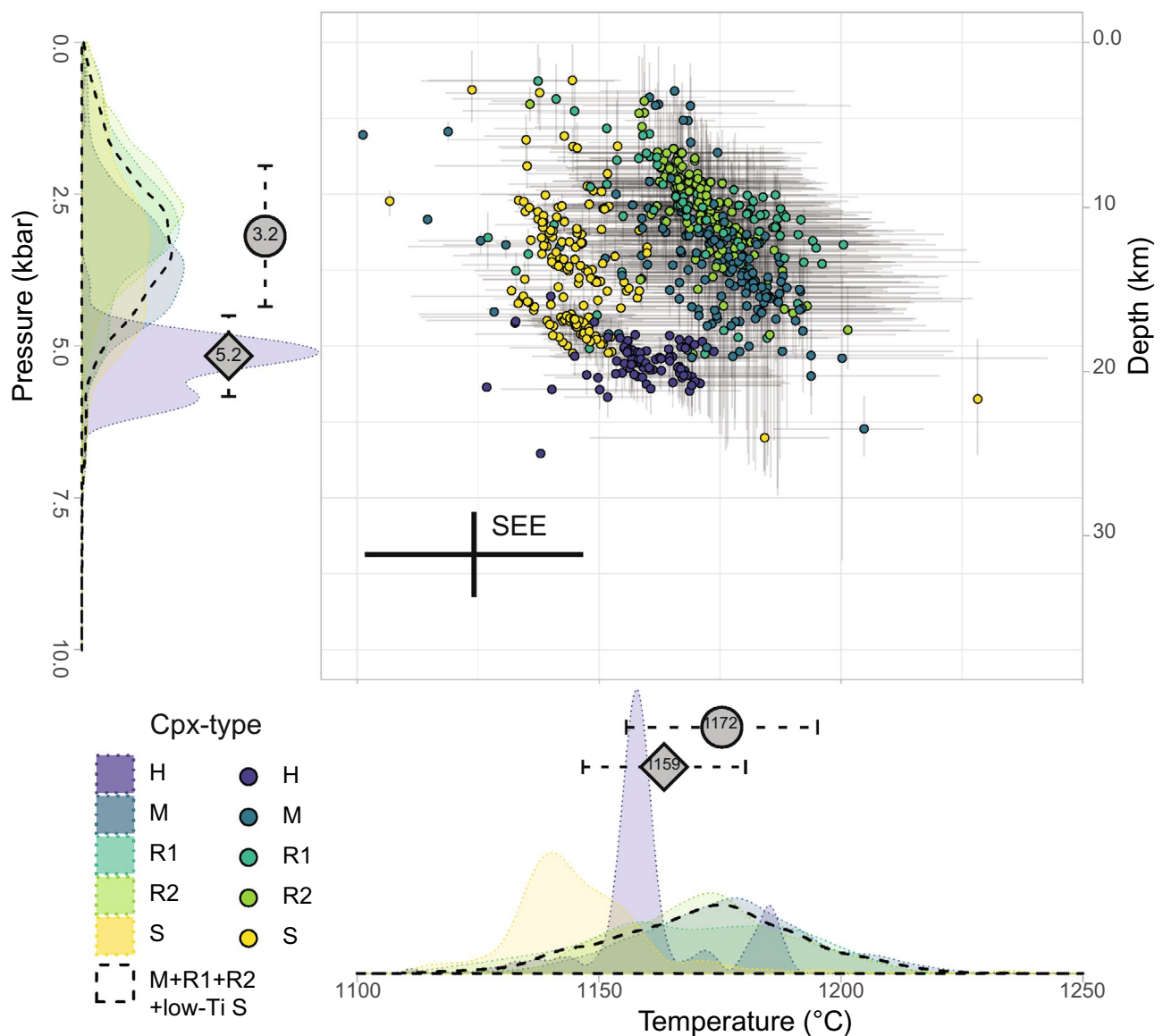


**Fig. 9** Pressures and temperatures of crystallization for all equilibrium cpx-whole-rock pairs, obtained through use of the method by Neave and Putirka (2017). Individual point data represent distinctive crystal measurements. Shaded error bars represent the range of calculated pressures and temperatures resulting from multiple equilibrium whole-rock matches. The 45 °C SEE of Eq. 33 of Putirka (2008) and 1.4 kbar SEE of the barometric equation of Neave and Putirka (2017)

are also displayed. Kernel distribution diagrams for each cpx-type are displayed for temperature and pressures (shaded coloured regions), with a combined distribution (excluding High-Ti sector zones and H-type crystals) also reported (dashed line). An overall mean (also excluding High-Ti sectors and H-types) is displayed together with its standard deviation (filled circle). The same approach is performed for H-type cpx (filled diamond)

R2-, and M-type cpx of the shield phase, covering a higher temperature ( $1174 \pm 18.4$  °C), intermediate pressure range ( $3.3 \pm 1.1$  kbar) (Fig. 9). The combination of low-Ti zones of S-type cpx and this major array result in an overall distribution peaking at a mean of  $3.2 \pm 1.2$  kbar, in line with the 3 kbar pressures used for rhyolite-MELTS modelling and associated 1234 °C onset of cpx crystallization. All reported pressures and temperatures following these models are additionally subject to their respective SEEs.

Use of the Putirka et al. (1996) model adjusted for over-estimation (see section on geothermobarometry methods) results in similarly extensive array of R1-, R2-, and M-type cpx, displaced to slightly higher pressures ( $4.3 \pm 1.5$  kbar) and temperatures ( $1192 \pm 18.4$  °C), which are nevertheless in range of the conditions predicted by rhyolite-MELTS modelling, especially when considering the 1.22 kbar and 34 °C SEEs. The few hawaiite pairs matched with this model report conditions more in line with the large array ( $4.4 \pm 1.4$ ), though displaced to lower temperatures ( $1157 \pm 12$  °C).

Combining both arrays as well as their standard deviations and respective SEEs, the plumbing system pressure can, in its broadest sense, be constrained to a range of 0.6–7 kbar.

### Trace element equilibria

Out of the selection of major-element equilibrated cpx-WR pairs, select crystals were measured for trace element equilibrium tests. Within this selection, we consider 12 of 18 to be within reasonable degrees of equilibrium, given the significant range of  $D_i$  values resulting from error propagation (Fig. 11b, d, g, j–r). M-type cpx are most well represented among these pairs, followed by R1 and R2 types, and finally, the few measurements performed on S- (only low-Ti sectors) and H-types. Pairs considered too far from equilibrium (Fig. 11a, c, e, f, h, i) display very limited overlap with the calculated ranges of partition coefficients, despite being in major element equilibrium. Pressures reported for equilibrated pairs are consistently in the range of 2.5–5.1 kbar (including  $1\sigma$  ranges), with the exception of DB07-013's pyroxene 5 (Fig. 11g), which reports a pressure of  $1.8 \pm 0.7$  kbar. It is noteworthy that calculated  $D_i$  for light rare earth elements La and Ce are consistently overestimated, which we attribute to higher uncertainties on LA-ICP-MS measurements for elements on the outer edges of the REE spectrum. This reasoning is then also applied to frequent underestimations of  $D_{Lu}$ .

## Discussion

### Crystal inheritance and differentiation processes

The mineralogical and geochemical diversity found in Hoya Island igneous rocks and associated cpx provide an important insight into the fractionation processes in the magmatic plumbing system of an ocean island. Populations of petrographically and chemically distinct cpx indicate for magma- or crystal-melt mixing in a variety of studied whole-rock samples, and support the presence of multiple magmatic reservoirs associated with distinct crystallization conditions. The inherited nature of the studied cpx phenocrysts is often supported by petrographic observations, in particular the rounding of crystals and the development of optically and chemically contrasted rims around otherwise unzoned cores (Bender et al. 1978) (Supplementary Materials 1, Fig. S14). According to our equilibrium calculations based on the works of Neave and Putirka (2017) and Putirka et al. (1996), all but M-type crystals most likely grew in melts other than their carrier liquids, which are either compositionally similar

(R2-types) or highly contrasted (R1-types). Accordingly, crystal mobility in the studied igneous rocks is best exemplified by R1-type cpx found in the olivine-rich picrites, which provide textural (dissolution-driven rounding), chemical (growth of singular or multiple crystal rims; Supplementary Materials 1, Fig. S14), and geothermobarometric evidence for their pre-eruptive mobility (equilibrium with unreported Mg-rich melts).

In general, the occurrence of picrites is associated with either direct extrusion of high-Mg magmas, or the accumulation of Mg-rich phases in a low-Mg magma (Révillon et al. 1999; Kerr and Arndt, 2001). In line with previous studies of Hoya picrites (Gazel et al. 2018), our results show that the whole rock and mineralogical composition of these igneous rocks require significant addition of olivine (and R1-type pyroxene) to parental to moderately differentiated basaltic melts ( $Mg\# = 49–71$ ). Although picrites were emplaced at different times of the shield stage of the island (Buchs et al. 2011), R1-type cpx, which are compositionally unique among all analysed cpx, are only found in these lavas. This suggests there were similar dynamics in the plumbing system of the island during formation of the picrites (transitional tholeiitic shield stage), before transition to the post-shield alkaline phase that is recorded by hawaiite lavas and dykes. The high  $Mg\#$  of R1-type cpx and their association with abundant olivine in the picrites suggest that these cpx were extracted from cumulates or cumulate-dominated parts of a mush system formed during the early stages of differentiation of parental melts, of which no representative composition is available. Such a mechanism has been previously proposed for Fuerteventura, where cumulate formation during magma ascent produces cpx with resorbed cores and progressively increases local viscosity, which in turn decreases the frequency of eruption of crystal-rich lavas (Tornare et al. 2016).

Based on our equilibrium and P-T calculations, this would have occurred in a melt/mush domain at intermediate depth, based on the most frequently reported pressure range among all shield-stage cpx ( $3.2 \pm 1.2$  kbar,  $SEE = 1.4$  kbar; Figs. 9, 11). Trace element equilibria additionally argue for such a range, reporting pressures of 1.1–5.1 kbar for the whole dataset. Crystals accumulated in this reservoir were subsequently extracted only in response to an eruption trigger providing sufficient buoyancy to the crystal-rich melt, such as mafic recharge by a  $CO_2$ -rich melt (e.g., Anderson, 1995). This interpretation is consistent with the low abundance of picrites at Hoya Island (Buchs et al. 2011) as well as the lack of R1-type pyroxenes and rounded olivines in the more differentiated (basaltic) rocks considered in this study. Dismemberment and extraction of cumulus crystals could

have been triggered by mafic recharge (Neumann et al. 1999; Nakagawa et al. 2002; Forni et al. 2018), significant magmatic differentiation triggering exsolution of gaseous phases (Cañón-Tapia, 2014), or gravitational destabilization of the inherently unstable mush network (Christopher et al. 2015; Sparks et al. 2018). Among these, melt injections (caused by or triggering mush destabilization) are judged to be the most likely, since these also provide an explanation for resorption-regrowth zoning observed in some R1-type crystals (Supplementary Materials 1, Fig. S14), and the combination of S-type and R1-type crystals within sample DB06-086.

Similarly, M-type cpx provide another, significant example of zoning which supports the frequent injection of new melt batches into the plumbing system of Hoya Island. Oscillatory-zoned augites have been explained through both intrinsic and extrinsic crystallization mechanisms (L'Heureux 1993; Elardo and Shearer 2014), a possible intrinsic mechanism being solute trapping (L'Heureux 1993; Elardo and Shearer 2014). This mechanism may occur when crystallization rates overtake diffusion rates, causing the crystal to preferentially accommodate more incompatible elements in a so-called 'boundary layer'. However, this mechanism produces micron-sized zone bands that are much smaller than those observed in the M-type cpx (Fig. 6a). In contrast, extrinsic control such as crystal convection, unstable conduit flow, and magma injection (Shimizu and Le Roex 1986; Shore and Fowler 1996; Ginibre et al. 2002; Humphreys et al. 2006; Elardo and Shearer 2014) can produce growth bands of a size comparable to those observed in M-type cpx (~10–15 µm), and would explain the alternation of Mg-rich and Mg-poor growth zones. Crystal convection requires a relatively large, liquid-dominated, and chemically heterogeneous magma chamber, which is at odds with our evidence for a mush rich plumbing system, as well as growing scientific consensus about the nature of magmatic reservoirs (Cashman et al. 2017). Unstable conduit flow could produce growth bands similar to those observed in M-type cpx, but this mechanism does not account for large chemical variations of the studied cpx, and this mechanism has thus far only been proven viable for plagioclase zoning (Humphreys et al. 2006). Therefore, we infer that the injection and/or movement of magmas due to gravitational destabilization of the crystal mush or simple mafic recharge is the most likely mechanism that could have led to the formation of the atypical oscillatory zoning of M-type cpx. In this interpretation, small M-type growing crystals become temporarily stalled in distinct parts of the plumbing system during their ascent through the oceanic lithosphere and intraplate volcano.

This interpretation is consistent with the large variety of whole-rock compositions in equilibrium with individual bands, while still allowing for equilibrium crystallization as is argued for by their euhedral crystal habit and geothermobarometric results. In a similar fashion, these minerals can form their particular textures through repeated injection of melts into a crystal mush system before being eventually dislodged and entrained within the magma towards the surface (e.g., Tornare et al. 2016). The small size of the M-type crystals and their oscillatory zoning indicate that the exposure time to compositionally contrasted melts was likely limited, as would be expected in a frequently replenished crystal mush system. Despite our samples not exhibiting reactive porous flow textures that are typical of some crystal mush networks (Lissenberg and Macleod 2016), many of our petrographic and geochemical observations support extensive magma mixing and crystal reworking in an open plumbing system, where crystal mushes can undergo both (background) percolative, reactive flow and periodic overturn (Christopher et al. 2015; Lissenberg and Macleod 2016; Cashman et al. 2017; Sparks et al. 2018).

Despite this evidence for inter-reservoir crystal mobility, agreements between rhyolite-MELTS modelling, geothermobarometric calculations, and trace element equilibria indicate the majority of the reservoir domains of Hoya Island to be limited to a restricted pressure range of 0.6–7.0 kbar (Figs. 9, 10, 11, including standard deviations and SEEs), with a mean pressure of  $3.2 \pm 1.2$  kbar and additional cut-off point at 6.5 kbar based on trace element equilibria. These conditions appear unchanged between the shield- and post-shield-phase, as far as the accuracy of our modelling can accurately discern. Although H-type cpx are indeed more jadeite-rich (Table 1) and consistently report slightly higher pressures of crystallization (Figs. 9, 10), due to extensive error propagation associated with the geothermobarometric approach, it is more likely for these features to be a result of their more alkali-rich equilibrium melt compositions. The H-type crystals are thus interpreted to have formed at similar pressures, but in the presence of more evolved, potentially water bearing melts, as also evidenced by their lower temperatures of crystallization (Figs. 9, 10) and agreement with 3 kbar hydrous rhyolite-MELTS models.

### Disequilibrium crystallization at Hoya Island

Though a significant amount of disequilibrium between carrier liquids and phenocrysts can be explained through crystal mobility as explained above, select converging observations

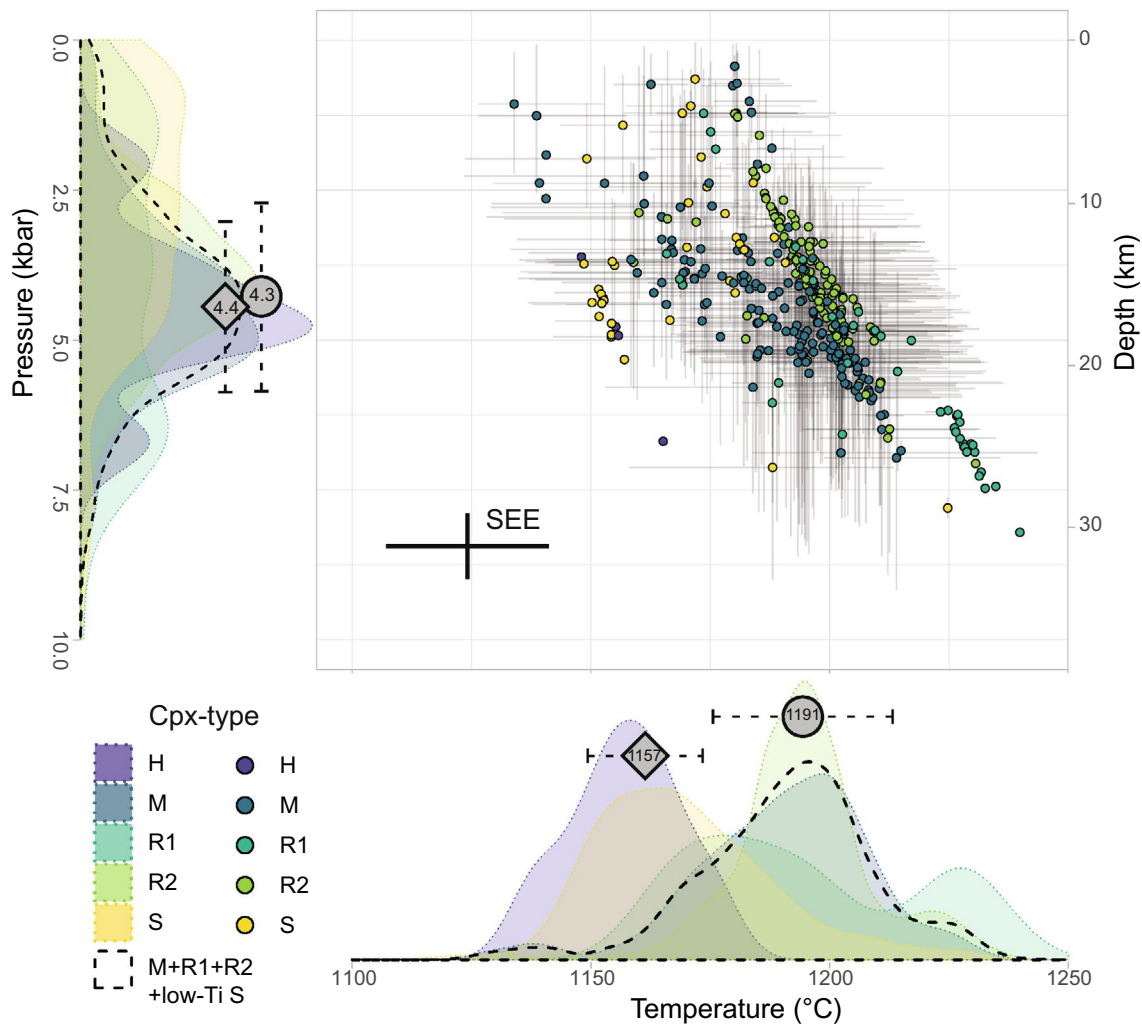


**Fig. 10** Pressures and temperatures of crystallization for all equilibrium cpx-whole-rock pairs, obtained through use of an iterative method adapted from Neave and Putirka (2017) but using the thermobarometric equations of Putirka et al. (1996) adjusted for overestimation (see section on geothermobarometry methods). Individual point data represent distinctive crystal measurements. Shaded error bars represent the range of calculated pressures and temperatures resulting from multiple equilibrium whole-rock matches. The 34 °C SEE of equation T2 of Putirka et al. (1996) and 1.22 kbar SEE of equation

P1 of Putirka et al. (1996) are also displayed. Kernel distribution diagrams for each cpx-type are displayed for temperature and pressures (shaded coloured regions), with a combined distribution (excluding High-Ti sector zones and H-type crystals) also reported (dashed line). An overall mean (also excluding High-Ti sectors and H-types) is displayed together with its standard deviation (filled circle). The same approach is performed for H-type cpx (filled diamond). A separate version uncorrected for pressure overestimation can be found in Supplementary Materials 1, Fig. S17

additionally support the occurrence of crystal growth under chemical disequilibrium in the magma plumbing system of Hoya Island.

This is most directly evidenced by the occurrence of S-type cpx in the picrite series. Chemical zoning like that observed in S-type cpx has been frequently documented in natural samples (e.g., Nakamura 1973; Claeason et al. 2007) and is not uncommon in experimental run products (Hart and Dunn 1993; Skulski et al. 1994; Lofgren et al. 2006; Schwandt and McKay 2006). Sector

zoning produced by rapid disequilibrium crystal growth most closely resembles our S-type cpx (Schwandt and McKay 2006). Such sector-zoned crystals can form from a supercooled magma at any cooling rate when nucleation points are available. The rapid growth of cpx in these conditions leads to high concentrations of Al in 001 faces, which results in incorporation of highly charged cations (e.g.,  $\text{Ti}^{4+}$ ,  $\text{REE}^{3+}$ ,  $\text{HFSE}^{4+}$ ) to maintain charge balance (McKay et al. 1994; Watson and Liang 1995; Lofgren et al. 2006; Schwandt and McKay 2006; Mollo et al. 2013b).

These crystallization conditions are consistent with our geochemical observations (e.g., Ti and REE contents) of S-type cpx. In addition, chadacrysts of plagioclase observed in these cpx (Fig. 3f) could represent nucleation points in the supercooled liquid. The required sub-solidus temperatures may be induced by either gas exsolution during ascent (Sparks 2003), or mixing with a more differentiated, low temperature melt (Hibbard 1981; Frost and Mahood 1987). At Hoya Island, co-occurrence of high-Mg R1-type and low-Mg S-type cpx in DB06-086 picrite supports the development of sector-zoned cpx in response to mixing of picritic magmas within a plagioclase-dominated, lower temperature melt reservoir.

### Implications from P-T and trace element melt-cpx modelling

The petrographic features reported for the lithologies of Hoya Island provide sufficient evidence for displacement of crystals from their original melts, which complicates the use of geothermobarometric models which require both melt and crystal compositions. Nevertheless, by combining petrographic evidence with major- and trace equilibrium calculations, as well as rhyolite-MELTS modelling, careful geothermobarometric calculations describe a consistent image of the structure of the Hoya Island plumbing system and processes active therein. With the exception of the formation of sector zoned cpx crystals, fractionation in this ocean island setting follows that of equilibrium crystallization in a frequently replenished mush-dominated system at relatively low pressures (0.6–7.0 kbar, all data, including SEE). Though it could be interpreted that the plumbing system extends throughout this pressure range, we would instead argue that the range of conditions reflects the significant uncertainties introduced by iteratively solving a variety of equations each with their own associated errors. Nevertheless, consistency between results from both crystal- and whole-rock-based approaches allows for a rough interpretation of the location of the plumbing system, which is in good agreement with previous studies from similar magmatic systems (e.g., Geist et al. 1998; Meletlidis et al. 2012; Zanon and Frezzotti 2013; Dorais and Buchs, 2019). Storage regions for tholeiitic shield-stage and alkaline post-shield stage magmas are indicated at an interval of 2–23 km depth with the majority of the data indicating a range between 2 and 19 km ( $3.2 \pm 2.6$  kbar, including SEE and using a density of  $3.3 \text{ g/cm}^3$ ). Such crystallization depths correspond to lower crustal or upper mantle levels, assuming a crustal thickness similar to the thickest areas at the modern Galapagos hotspot (Feighner and Richards 1994).

Similar to what is observed in arc volcanoes (e.g., Streck et al. 2005), mid-ocean ridges (e.g., Costa et al. 2010) and oceanic islands in slow-moving plate settings (e.g., Tornare et al. 2016), our results indicate that whole-rock data from Pacific oceanic islands (i.e., oceanic intraplate setting on a fast-moving lithosphere) do not represent simple melt batches from which crystals slowly crystallized. A combined approach of whole-rock and crystal chemistries in terms of both major and trace elements is, therefore, the most accurate approach to establish crystallization conditions.

### Conclusions

Petrographic and geochemical constraints from whole-rock samples of picrites, basalts and hawaiites and their associated cpx phenocrysts show that the formation of Hoya Island during transition from its shield (transitional tholeiitic) to post-shield (alkaline) phases was most likely associated with the development of a complex intra-lithospheric crystal mush-network. Frequent mafic recharge, crystal fractionation, mush destabilisation, and mixing between distinct mush reservoirs caused displacement of crystals from their original carrier liquids, ultimately leading to widespread obscuration of the original compositions of equilibrium melts in this open magmatic system. Fast-paced recharge and associated crystal displacement in the plumbing system of Hoya Island are evidenced by clinopyroxene phenocrysts with sectoral and oscillatory zoning, as well as multiple-resorption textures. Olivine and high-Mg clinopyroxene phenocrysts entrained by basaltic melts to form picrites indicate that mafic recharge events break loose previously formed cumulates/crystal mushes. This was accompanied by undercooling and rapid crystallization of magmas following mixing in shallow reservoirs, as supported by sector-zoned clinopyroxene phenocrysts found in basalts and the glassy matrix in crystal-rich picrites. A combination of rhyolite-MELTS modelling, careful equilibrium evaluations, and clinopyroxene geothermobarometry allow for approximation of the plumbing system depth to 2–23 km, with a high likelihood of being at < 19 km depth. No clear evidence is found for post-shield stage migration of magma chambers to deeper levels. The abundance of cpx-carrier liquid disequilibrium documented in Hoya Island is an important result of our study that strongly supports extensive magma mixing, mafic recharge, and crystal entrainment in an open (crystal-mush dominated) magmatic system. Overall, our results highlight the potential complexities of interpreting magmatic systems, and the need to use an extensive, detailed petrographical and mineral geochemical analysis to better constrain petrological interpretations.

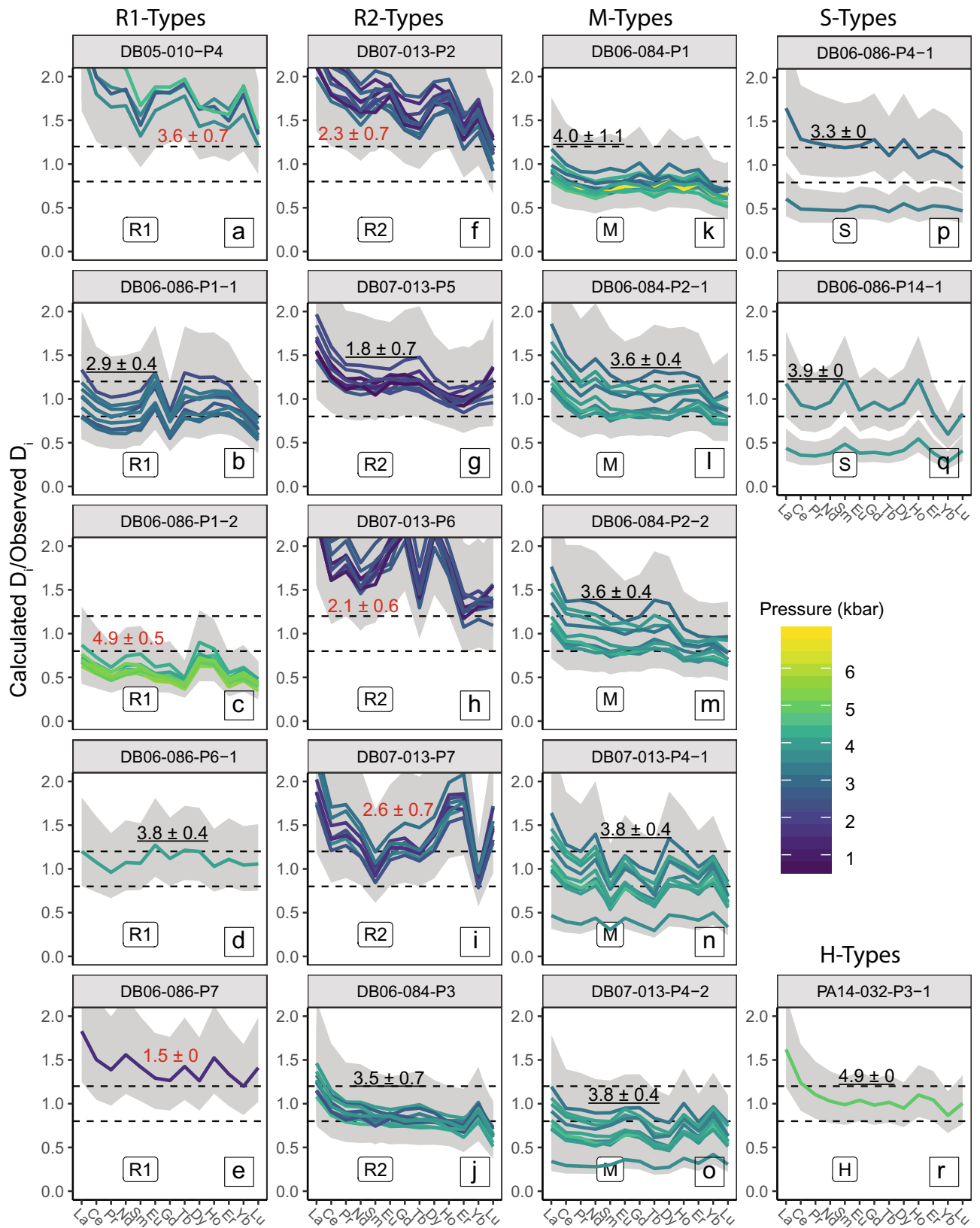


**Fig. 11** Degrees of trace element equilibrium for distinct cpx trace element measurements per cpx-type (columns, also listed per frame) following the approach of Wood and Blundy (1997). Each panel represents a cpx trace element measurement of which the major element composition was matched with one or more whole-rocks. Coloured lines represent individual whole-rock matches in terms of the ratio of their calculated partition coefficients (using their Mg# and calculated P-T conditions) over the observed partition coefficient. Temperatures and pressures used in the model by Wood and Blundy (1997) result from geothermobarometric calculations following the approaches of Neave and Putirka (2017) (R1, R2, M, and S-types) and Putirka et al. (1996) (H-types). Only low-Ti sectors of S-type crystals are considered. Each whole-rock line is accompanied by a shaded error region which represents the range of possible partition coefficient values when taking into account the SEEs of the used barometric and thermobarometric models (see section on geothermobarometry methods). Dashed lines represent a 20% equilibrium envelope. Mean pressures and 1 $\sigma$  standard deviations are noted next to the groups of overlapping closest-to-equilibrium whole-rock lines, which are underlined for samples considered to be within reasonable degrees of trace element equilibrium. Numbering follows a ‘WR – P (cpx number) – Analysis number’ format

**Supplementary Information** The online version contains supplementary material available at <https://doi.org/10.1007/s00410-022-01894-w>.

**Acknowledgements** We thank Cardiff University’s professional service staff Anthony Oldroyd and Dr. Duncan Muir for their help with sample preparation and SEM analysis, respectively. We are grateful to Dr. Stuart Kearns of Bristol University for his guidance in EMP analysis. Thanks are given to Ing. Helen de Waard of Utrecht University with her assistance with LA-ICP-MS. Lastly, we would like to thank Dr. David A. Neave for his external consultation on geothermobarometry. JB acknowledges support from a Royal Society Research Professorship. We would additionally like to thank Francesca Forni, Martin Streck, Silvio Mollo, an anonymous reviewer, and the handling editor for their invaluable feedback which allowed us to greatly improve this work.

**Author contributions** SMM collected new data, conducted the research, and prepared the manuscript and figures. DMB contributed to the research and manuscript/figures design. PRDM and JDB helped with data interpretation and manuscript improvements.

**Funding** This study benefited from grant #GEFNE137-15 of the National Geographic Society.

**Availability of data and materials** Data are available as supplementary electronic files. Materials remain available at the time of publication (contact D.M. Buchs for enquiries).

**Code availability** Not applicable.

## Declarations

**Conflict of interest** Not applicable.

**Open Access** This article is licensed under a Creative Commons Attribution 4.0 International License, which permits use, sharing, adaptation, distribution and reproduction in any medium or format, as long as you give appropriate credit to the original author(s) and the source, provide a link to the Creative Commons licence, and indicate if changes were made. The images or other third party material in this article are included in the article’s Creative Commons licence, unless indicated

otherwise in a credit line to the material. If material is not included in the article’s Creative Commons licence and your intended use is not permitted by statutory regulation or exceeds the permitted use, you will need to obtain permission directly from the copyright holder. To view a copy of this licence, visit <http://creativecommons.org/licenses/by/4.0/>.

## References

- Anderson AT (1995) CO<sub>2</sub> and the eruptibility of picrite and komatiite. *Lithos* 34(1–3):19–25
- Bender JF, Hodges FN, Bence AE (1978) Petrogenesis of basalts from the project FAMOUS area: experimental study from 0 to 15 kbars. *Earth Planet Sci Lett* 41(3):277–302
- Brounce M, Stolper E, Eiler J (2017) Redox variations in Mauna Kea lavas, the oxygen fugacity of the Hawaiian plume, and the role of volcanic gases in Earth’s oxygenation. *Proc Natl Acad Sci* 114(34):8997–9002
- Buchs DM, Arculus RJ, Baumgartner PO, Baumgartner-Mora C, Ulianov A (2010) Late Cretaceous arc development on the SW margin of the Caribbean plate: insights from the Golfito, Costa Rica, and Azuero Panama, complexes. *Geochem Geophys Geosyst* 11(7):Q07S24
- Buchs DM, Arculus RJ, Baumgartner PO, Ulianov A (2011) Oceanic intraplate volcanoes exposed: example from seamounts accreted in Panama. *Geology* 39(4):335–338
- Buchs DM, Kerr AC, Brims JC, Zapata-Villada JP, Correa-Restrepo T, Rodríguez G (2018a) Evidence for subaerial development of the Caribbean oceanic plateau in the Late Cretaceous and palaeo-environmental implications. *Earth Planet Sci Lett* 499:62–73
- Buchs DM, Williams R, Sano S-I, Wright VP (2018b) Non-Hawaiian lithostratigraphy of Louisville seamounts and the formation of high-latitude oceanic islands and guyots. *J Volcanol Geoth Res* 356:1–23
- Cameron M, Papike JJ (1981) Structural and chemical variations in pyroxenes. *Am Miner* 66:1–50
- Cañón-Tapia E (2014) Volcanic eruption triggers: a hierarchical classification. *Earth Sci Rev* 129:100–119
- Cashman K, Sparks RSJ, Blundy J (2017) Vertically extensive and unstable magmatic systems: a unified view of igneous processes. *Science* 355(6331):1280
- Christopher TE, Blundy J, Cashman K, Cole P, Edmonds M, Smith PJ, Sparks RSJ, Strinton A (2015) Crustal-scale degassing due to magma system destabilization and magma-gas decoupling at Soufrière Hills Volcano, Montserrat. *Geochem Geophys Geosyst* 16:2797–2811
- Claeson DT, Meurer WP, Högalm KJ, Larson S-Å (2007) Using LA-ICP-MS mapping and sector zonation to understand growth and trace-element partitioning in sector-zoned clinopyroxene oikocrysts from the Norra Ulvö Gabbro, Sweden. *J Petrol* 48(4):711–728
- Clague DA, Dalrymple GB (1987) The Hawaiian- Emperor volcanic chain. Part I. Geologic evolution. *US Geological Survey Professional Paper*, 1350(1): 5–54.
- Costa F, Coogan LA, Chakraborty S (2010) The time scales of magma mixing and mingling involving primitive melts and melt-mush interaction at mid-ocean ridges. *Contrib Miner Petrol* 159(3):371–387
- Cottrell E, Birner SK, Brounce M, David FA, Waters LE, Kelley KA (2021) Oxygen fugacity across tectonic settings. In: Neuvill DR, Moretti R (eds) *Magma redox geochemistry*. Wiley, pp 33–61
- Davis AS, Clague DA, Bohron WA, Dalrymple GB, Greene HG (2002) Seamounts at the continental margin of California: a

- different kind of oceanic intraplate volcanism. *Bull Geol Soc Am* 114(3):316–333
- Dobosi G, Fodor RV (1992) Magma fractionation, replenishment, and mixing as inferred from green-core clinopyroxenes in Pliocene basanite, southern Slovakia. *Lithos* 28:133–150
- Dorais MJ, Buchs DM (2019) Mineralogical characterization of rejuvenated magmatism at Burton Guyot, Louisville Seamount trail. *Contrib Mineral Petrol* 174(8):66
- Elardo SM, Shearer CK (2014) Magma chamber dynamics recorded by oscillatory zoning in pyroxene and olivine phenocrysts in basaltic lunar meteorite Northwest Africa 032. *Am Miner* 99(2–3):355–368
- Feighner MA, Richards MA (1994) Lithospheric structure and compensation mechanisms of the Galapagos Archipelago. *J Geophys Res* 99(B4):6711–6729
- Forni F, Degruyter W, Bachmann O, De Astis G, Mollo S (2018) Long-Term magmatic evolution reveals the beginning of a new caldera cycle at Campi Flegrei. *Sci Adv* 4(11):eaat9401
- Frost TP, Mahood GA (1987) Field, chemical, and physical constraints on mafic–felsic magma interaction in the Lamarck Granodiorite, Sierra Nevada, California (USA). *Geol Soc Am Bull* 99(2):272–291
- Gazel E, Trela J, Bizimis M, Sobolev A, Batanova V, Class C, Jicha B (2018) Long-lived source heterogeneities in the Galapagos Mantle Plume. *Geochem Geophys Geosyst* 19(8):2764–2779
- Geist D, Naumann T, Larson P (1998) Evolution of Galapagos magmas: mantle and crustal fractionation without assimilation. *J Petrol* 39(5):953–971
- Ginibre C, Worner G, Kronz A (2002) Minor- and trace-element zoning in plagioclase: implications for magma chamber processes at Parinacota volcano, northern Chile. *Contrib Mineral Petrol* 143(3):300–315
- Gualda GAR, Ghiorsio MS, Lemons RV, Carley TL (2012) Rhyolite-MELTS: a modified calibration of MELTS optimized for silica-rich, fluid-bearing magmatic systems. *J Petrol* 53:875–890
- Hart SR, Dunn T (1993) Experimental cpx/melt partitioning of 24 trace elements. *Contrib Mineral Petrol* 113(1):1–8
- Hibbard MJ (1981) The magma mixing origin of mantled feldspars. *Contrib Mineral Petrol* 76(2):158–170
- Hill E, Blundy JD, Wood BJ (2011) Clinopyroxene-melt trace element partitioning and the development of a predictive model for HFSE and Sc. *Contrib Mineral Petrol* 161(3):423–438
- Hill E, Blundy JD, Wood BJ (2012) Erratum to: clinopyroxene-melt trace element partitioning and the development of a predictive model for HFSE and Sc. *Contrib Mineral Petrol* 163:563–565
- Hoernle K, van den Boogaard P, Werner R, Lissinna B, Alverado G, Garbe-Schönberg D (2002) Missing history (16–71 Ma) of the Galápagos hotspot: implications for the tectonic and biological evolution of the Americas. *Geology* 30(9):795–798
- Humphreys MCS, Blundy JD, Sparks RSJ (2006) Magma evolution and open-system processes at Shiveluch volcano: insights from phenocryst zoning. *J Petrol* 47(12):2303–2334
- Kerr AC, Arndt NT (2001) A note on the IUGS reclassification of the high-Mg and picritic volcanic rocks. *J Petrol* 42(11):2169–2171
- Klügel A, Hansteen TH, Galipp K (2005) Magma storage and underplating beneath Cumbre Vieja volcano, La Palma (Canary Islands). *Earth Planet Sci Lett* 236(1–2):211–226
- Konter JG, Staudigel H, Blichert-Toft J, Hanan BB, Polvé M, Davies GR, Shimizu N, Schiffman P (2009) Geochemical stages at Jasper seamount and the origin of intraplate volcanoes. *Geochem Geophys Geosyst* 10(2):Q02001
- Kress VC, Carmichael ISE (1991) The compressibility of silicate liquids containing Fe<sub>2</sub>O<sub>3</sub> and the effect of composition, temperature, oxygen fugacity and pressure on their redox states. *Contrib Mineral Petrol* 108(1–2):82–92
- Le Bas M, Maitre R, Streckeisen A, Zanettin B (1986) A chemical classification of volcanic rocks based on the total alkali-silica diagram. *J Petrol* 27:745–750
- L’Heureux I (1993) Oscillatory zoning in crystal growth: a constitutional undercooling mechanism. *Phys Rev E* 48(6):4460–4469
- Lindsley H (1983) Pyroxene thermometry. *Am Miner* 68:477–493
- Lissenberg CJ, MacLeod CJ (2016) A reactive porous flow control on mid-ocean ridge magmatic evolution. *J Petrol* 57(11–12):2195–2220 (egw074)
- Lofgren GE, Huss GR, Wasserburg GJ (2006) An experimental study of trace-element partitioning between Ti-Al-clinopyroxene and melt: equilibrium and kinetic effects including sector zoning. *Am Miner* 91(10):1596–1606
- Marks M, Halama R, Wenzel T, Markl G (2004) Trace element variations in clinopyroxene and amphibole from alkaline to peralkaline syenites and granites: implications for mineral-melt trace element partitioning. *Chem Geol* 211:185–215
- Marsh BD (1996) Solidification fronts and magmatic evolution. *Mineral Mag* 60(398):5–40
- McDonough WF, Sun SS (1995) The composition of the Earth. *Chem Geol* 120(3–4):223–253
- McKay G, Le L, Wagstaff J, Crozaz G (1994) Experimental partitioning of rare earth elements and strontium: constraints on petrogenesis and redox conditions during crystallization of Antarctic angrite Lewis Cliff 86010. *Geochim Cosmochim Acta* 58(13):2911–2919
- Meletlidis S, Di Roberto A, Pompilio M, Bertagnini A, Iribarren I, Felpeto A, Torres PA, D’Oriano C (2012) Xenopumices from the 2011–2012 submarine eruption of El Hierro (Canary Islands, Spain): constraints on the plumbing system and magma ascent. *Geophys Res Lett* 39(17):L17302
- Mollo S, Putirka K, Misiti V, Soligo M, Scarlato P (2013a) A new test for equilibrium based on clinopyroxene-melt pairs: clues on the solidification temperatures of Etnean alkaline melts at post-eruptive conditions. *Chem Geol* 352:92–100
- Mollo S, Blundy JD, Iezzi G, Scarlato P, Langone A (2013b) The partitioning of trace elements between clinopyroxene and trachybasaltic melt during rapid cooling and crystal growth. *Contrib Mineral Petrol* 166(6):1633–1654
- Morimoto N (1988) Nomenclature of pyroxenes. *Mineral Petrol* 39(1):55–76
- Nakagawa M, Wada K, Wood CP (2002) Mixed magmas, mush chambers and eruption triggers: evidence from zoned clinopyroxene phenocrysts in Andesitic Scoria from the 1995 eruptions of Ruapehu volcano, New Zealand. *J Petrol* 43(12):2279–2303
- Nakamura Y (1973) Origin of sector zoning of igneous clinopyroxenes. *Am Miner* 58:986–990
- Nakamura M (1995) Continuous mixing of crystal mush and replenished magma in the ongoing Unzen eruption. *Geology* 23(9):807–810
- Neave DA, Putirka KD (2017) A new clinopyroxene-liquid barometer, and implications for magma storage pressures under Icelandic rift zones. *Am Miner* 102(4):777–794
- Neave DA, Bali E, Guðfinnsson GH, Halldórsson SA, Kahl M, Schmidt A, Holtz F (2019) Clinopyroxene-liquid equilibria and geothermobarometry in natural and experimental tholeiites: the 2014–2015 Holuhraun eruption, Iceland. *J Petrol* 60(8):1653–1680
- Neumann E-R, Wulff-Pedersen E, Simonsen SL, Pearson NJ, Martí J, Mitjavila J (1999) Evidence for fractional crystallization of periodically refilled magma chambers in Tenerife, Canary Islands. *J Petrol* 40(7):1089–1123
- Putirka K (1997) Magma transport at Hawaii: inferences based on igneous thermobarometry. *Geology* 25(1):69–72
- Putirka KD (2008) Thermometers and barometers for volcanic systems. *Rev Mineral Geochem* 69:61–120

- Putirka K, Johnson M, Kinzler R, Longhi J, Walker D (1996) Thermo-barometry of mafic igneous rocks based on clinopyroxene-liquid equilibria 0–30 kbar. *Contrib Mineral Petrol* 123(1):92–108. <https://doi.org/10.1007/s004100050145>
- Révilion S, Arndt NT, Hallot E, Kerr AC, Tarney J (1999) Petrogenesis of picrites from the Caribbean Plateau and the North Atlantic magmatic province. *Lithos* 49(1–4):1–21
- Schindelin J, Arganda-Carreras I, Frise E, Kaynig V, Longair M, Pietzsch T, Preibisch S, Rueden C, Saalfeld S, Schmid B, Tinevez J-Y, White DJ, Hartenstein V, Eliceiri K, Tomancak P, Cardona A (2012) Fiji: an open-source platform for biological-image analysis. *Nat Methods* 9(7):676–682
- Schindelin J, Rueden CT, Hiner MC, Eliceiri KW (2015) The ImageJ ecosystem: an open platform for biomedical image analysis. *Mol Reprod Dev* 82(7–8):518–529
- Schwandt CS, Mckay GA (2006) Minor- and trace-element sector zoning in synthetic enstatite. *Am Miner* 91(10):1607–1615
- Shimizu N, Le Roex AP (1986) The chemical zoning of augite phenocrysts in alkaline basalts from Gough Island, South Atlantic. *J Volcanol Geoth Res* 29(1–4):159–188
- Shore M, Fowler AD (1996) Oscillatory zoning in minerals: a common phenomenon. *Can Mineral* 34(6):1111–1126
- Skulski T, Minarik W, Watson EB (1994) High-pressure experimental trace-element partitioning between clinopyroxene and basaltic melts. *Chem Geol* 117:127–147
- Sparks RSJ (2003) Dynamics of magma degassing. *Geol Soc Spec Pub* 213:5–22
- Sparks RSJ, Annen C, Blundy JD, Cashman KV, Rust AC, Jackson MD (2018) Formation and dynamics of magma reservoirs. *Phil Trans R Soc A* 377:20180019
- Staudigel H, Clague DA (2010) The geological history of deep-sea volcanoes: biosphere, hydrosphere, and lithosphere interactions. *Oceanography* 23(1):58–71
- Stone S, Niu Y (2009) Origin of compositional trends in clinopyroxene of oceanic gabbros and gabbroic rocks: a case study using data from ODP Hole 735B. *J Volcanol Geoth Res* 184(3–4):313–322
- Streck MJ, Dungan MA, Bussy F, Malavassi E (2005) Mineral inventory of continuously erupting basaltic andesites at Arenal volcano, Costa Rica: implications for interpreting monotonous, crystal-rich mafic arc stratigraphies. *J Volcanol Geoth Res* 140:133–155
- Stroncik NA, Klügel A, Hansteen TH (2009) The magmatic plumbing system beneath El Hierro (Canary Islands): constraints from phenocrysts and naturally quenched basaltic glasses in submarine rocks. *Contrib Miner Petrol* 157(5):593–607
- Tornare E, Pilet S, Bussy F (2016) Magma differentiation in vertical conduits revealed by the complementary study of plutonic and volcanic rocks from Fuerteventura. *J Petrol* 57(11–12):2221–2250
- Vander Auwera J, Namur O, Dutrieux A, Wilkinson CM, Ganerød M, Coumont V, Bolle O (2019) Mantle melting and magmatic processes under La Picada Stratovolcano (CSVZ, Chile). *J Petrol* 60(5):907–944
- Wang J, Wang Q, Dan W, Yang JH, Yang ZY, Sun P, Qi Y, Hu WL (2019) The role of clinopyroxene in amphibole fractionation of arc magmas: evidence from mafic intrusive rocks within the Gangdese arc, southern Tibet. *Lithos* 338:174–188
- Watson EB, Liang Y (1995) A simple model for sector zoning in slowly grown crystals: implications for growth rate and lattice diffusion, with emphasis on accessory minerals in crustal rocks. *Am Miner* 80:1179–1187
- Wood BJ, Blundy J (1997) A predictive model for rare earth element partitioning between clinopyroxene and anhydrous silicate melt. *Contrib Miner Petrol* 129:166–181
- Woodhead JD (1992) Temporal geochemical evolution in oceanic intra-plate volcanics: a case study from the Marquesas (French Polynesia) and comparison with other hotspots. *Contrib Miner Petrol* 111(4):458–467
- Zanon V, Frezzotti ML (2013) Magma storage and ascent conditions beneath Pico and Faial islands (Azores archipelago): a study on fluid inclusions. *Geochem Geophys Geosyst* 14(9):3494–3514

**Publisher's Note** Springer Nature remains neutral with regard to jurisdictional claims in published maps and institutional affiliations.